Hierarchical and size dependent mechanical properties of silica and silicon nanostructures inspired by diatom algae

by

Andre Phillipe Garcia

B.S., Civil Engineering and Environmental Engineering,
Summa Cum Laude, University of South Florida (2008)

Submitted to the Department of Civil and Environmental Engineering
in partial fulfillment of the requirements for the degree of

Master of Science

at the

MASSACHUSETTS INSTITUTE OF TECHNOLOGY

September 2010

Author .....
Department of Civil and Environmental Engineering
August 18, 2010

Certified by .....
Markus J. Buehler
Associate Professor of Civil and Environmental Engineering
Thesis Supervisor

Accepted by .....
Daniele Veneziano
Chairman, Departmental Committee for Graduate Students

Hierarchical and size dependent mechanical properties of silica and silicon nanostructures inspired by diatom algae

by

Andre Phillipe Garcia

Submitted to the Department of Civil and Environmental Engineering
on August 18, 2010, in partial fulfillment of the
requirements for the degree of
Master of Science in the field of Civil and Environmental Engineering

Abstract

Biology implements fundamental principles that allow for attractive mechanical properties, as observed in biomineralized structures. For example, diatom algae contain nanoporous hierarchical silicified shells that provide mechanical defense from predators and virus penetration. These shells generally have a morphology resembling honeycombs within honeycombs, meshes, or corrugated folds, and are surprisingly tough when compared to bulk silica, which is one of the most brittle materials known. However, the reason for the enhanced mechanical properties has remained elusive. Here, it is proposed that one reason for the superior mechanical properties lies in the geometric arrangement, size, and shape of the structures. By carrying out a series of molecular dynamics simulations with the first principles based reactive force field ReaxFF, it is shown that when concurrent mechanisms occur, such as shearing and crack arrest, toughness is optimally enhanced. This occurs, for example, when structures encompass two nanoscale levels of hierarchy: an array of thin walled foil silica structures, and a hierarchical arrangement of foil elements into a porous silica mesh structure. For wavy silica, unfolding mechanisms are achieved for increasing amplitude, and allow for greater ductility. Furthermore, these deformation mechanisms are governed by the size and shape of the structure. The ability to transform multiple mechanical properties, such as toughness, strength, and ductility, is extremely important when looking into future applications of nanoscale materials. Altering the mechanical properties of one of the most brittle and abundant minerals on earth, silica, allows a new window of opportunity for humanity to create applications and reinvent materials once thought to be impossible. The transferability of the concept allowing for massive transformation of mechanical responses, such as brittle to ductile or weak to tough, through geometric alterations at the nanoscale, is a profound discovery that may unleash a new paradigm in the way materials are designed.

Thesis Supervisor: Markus J. Buehler
Title: Associate Professor of Civil and Environmental Engineering

Acknowledgments

I would like to express my eternal gratitude for those who have influenced, guided, and educated me toward my ever expanding goals. My advisor, Professor Markus J. Buehler, is an inspiring mentor and a constant catalyst in my academic evolution, and for this I am deeply grateful. I would like to thank Dipanjan Sen for his fundamental mentorship and friendship. I appreciate all of my lab mates for their great companionship, and thank all those who have provided fruitful discussion and help: Sinan Keten, Raffaella Paparcone, Zhiping Xu, Zhao Qin, Andrea Nova, and Steve Cranford. Also, I am grateful for my family, a cornoerstone that supports me in all endeavors, challenges, and goals.

This research was funded by the National Science Foundation through a Graduate Research Fellowship, the Army Research Office (grant number W9-11NNF-06-1029), the Gates Millennium Scholars Program, and a graduate research fellowship awarded by the Department of Civil and Environmental Engineering at the Massachusetts Institute of Technology. Their support is greatly appreciated.

Dedicado a mi padre, Felipe Garcia.

Contents

List of journal publications

1. **A. P. Garcia**, M. J. Buehler, "Superductile, wavy silica nanostructures inspired by diatom algae", in submission.

2. D. Sen, **A. P. Garcia**, M. J. Buehler, "Mechanics of nano-honeycomb silica structures: A size-dependent brittle-to-ductile transition", in review.

3. **A. P. Garcia**, D. Sen, M. J. Buehler, "Hierarchical silica nanostructures inspired by diatom algae yield superior deformability, toughness and strength", accepted for publication in: *Metallurgical and Materials Transactions A*.

4. **A. P. Garcia**, M. J. Buehler, "Bioinspired nanoporous silicon provides great toughness at great deformability", *Computational Materials Science*, 48(2):303-309, 2010.

List of Figures

List of Tables

Chapter 1

Background

Since the dawn of civilization, nature been a source of countless inspiration. The impetus for discovery in many notable minds of the past, like Newton, da Vinci, and Darwin, has centered around nature and its fascinating characteristics. With the unfolding of time, nature has left its indelible impact in the design of man made structures. Presently, the field of biomimetics has come into the age of the nanoscale, offering an impressive array of inventions that redefine conventional thought. In this thesis, a systematic analysis of the mechanical properties of diatom inspired nanoscale mineralized structures is undertaken. As the future foundation of synthetic materials will rest on the shoulders of the nanoworld, this thesis will hopefully serve as a guiding light and motivation for the use of nanoscale minerals in conventional design paradigms and applications. The awe, magnitude, and beauty of the nanoworld is aptly embodied by the following quote:

"To see a world in a grain of sand, And a heaven in a wild flower,
Hold infinity in the palm of your hand, And eternity in an hour ..." -
William Blake [37]

1.1 The diatom

Although invisible to the naked eye, yet unconsciously implemented in structures throughout human history, diatoms have served as a silent backbone to human

civilization and play a role in cement, carbon sequestration, water filters, and oil [58, 31, 17, 28, 4, 56, 71]. The impressive arrays of diatom types and applications are shown in Figures 1-1, 1-2, 1-3, and 1-4 . But why have they served such an important role? The answer may lie at the nanoscale. Diatoms are micrometer sized algae with silicified, porous shells. Generally, these pores and surrounding walls have nanometer to micrometer dimensions and serve to protect the organism and sustain multiple biological functions. Examples of mechanical protection include preventing virus penetration, crushing from some predator's mandibles, or digestion [73, 38, 30].

Rather few experimental data has been collected on the mechanical properties of diatom shells, called frustules. Hamm *et al.* [39] used a glass needle to load and break diatom frustules in order to probe their mechanical response at failure. Their findings for the *F. kerguelensis* species revealed an elastic modulus of 22.4 GPa, and a maximum stress along the costae of 0.6 GPa (in tension) and 0.7 GPa (in compression). A comparison of the mechanical properties between different structural materials and diatom regions is found in Table 1.1. Other studies [60] have used AFM nanoindentation to study the nanoscale material properties of the porous frustule layers of diatoms, identifying pore sizes on the order of several tens of nanometers at the smallest levels in the hierarchy, with ultra-thin silica walls on the order of several nanometers. For *Coscinodiscus sp.* It was found that the porosity increased from the outer to the inner membrane. The pore size ranged from 45 ± 9, 192 ± 35, 1150 ± 130 nm for the cribellum, cribrum, and areola layers, respectively. Of the three layers, the cribellum had the lowest hardness and elastic modulus: 0.076 ± 0.034 GPa, and 3.40 ± 1.35 GPa, whereas the areola had the highest: 0.53 ± 0.13 GPa, and 15.61 ± 5.13 GPa, respectively [60, 59]. They observed that the variation of mechanical properties between the frustule layers could be influenced by the pore size, pore distance, porosity, and under different biomineralization processes.

The mechanical properties of diatoms and links to associated structural features has already been discussed in the literature. For instance, the raphid diatom has a raphe, which is a split in the frustule along its length with blunted ends, which helps to reduce stress concentrations [38, 39]. Further, many diatoms share a hexagonal

pattern to the frustules, which feature a high moment of inertia due to the large distance between the hexagon ledge and the hexagon centroid. A high moment of inertia increases the capacity of the structure to withstand deformation [39]. The material that composes the frustules is also important to the diatoms flexibility and toughness. For example, during the initial stages of frustules growth, silaffins and polyamines proteins co-precipitate with silicic acid found in the aqueous environment, thus forming a composite organic material [43, 52, 84, 77, 70]. The cross sectional shape of the outermost layer, the cribellum, are shallow domes with the tip pointing outward and the cribrum forms another dome pointing inward, similar to egg shells or hillocks. Connecting the base of the cribrum and areola is a wall type structure reminiscent of an I-beam. The lower base of the wall forms the surface of the areola. This I-beam shape is very common in macroscale engineering applications such as in steel I-beams used in construction of buildings, and offers an extremely efficient design due to its high moment of inertia, thus allowing for increased bending stiffness and greater shear resistance. From a structural point of view, domes are also used in engineering design due to their capacity to distribute compressive loads along the wall. Overall, the review of earlier structural and mechanical analyses reveals that diatoms are fascinating nanoscale structures that incorporate multiple engineering design concepts, perhaps resulting in an optimization of their mechanical stability.

Materials and diatom regions	**Strength (GPa)**	**Young's Modulus (GPa)**
cement (compression)	20 – 55	10 – 35
steel	0.2 – 1	200
Aluminum	0.1 – 0.2	70
Copper	0.2 – 0.4	110
Silicon	0.2	180
Silica	0.04 – 0.06	80 – 90
cribellum	0.042 – 0.11	2.05 – 4.75
cribrum	0.02 - 0.24	0.86 – 2.54
areola layers	0.4 – 0.66	10.48 – 20.74

Table 1.1: Comparison between structural materials and diatom regions (Data summarized from Ref. [60, 6]).

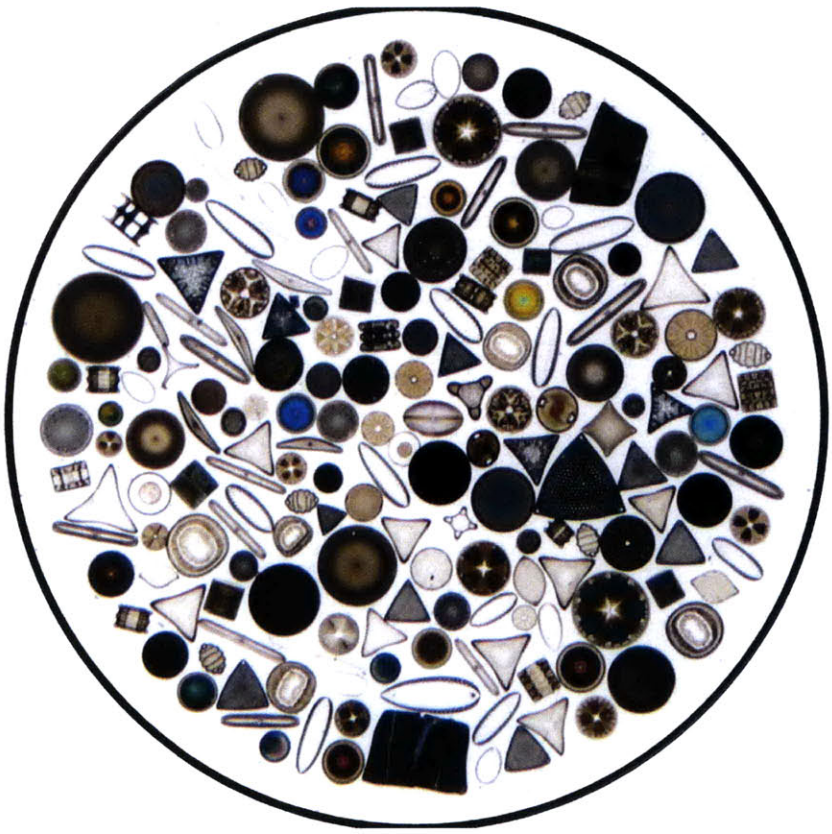

Figure 1-1: . These marine diatoms represent the wide array of diatom species, which reach up to approximately 100,000. Common diatom morphologies are circular, triangular, quadrilateral, and elliptical. Diatoms generally range from 2 – 2,000 μm in overall size [41]. Reprinted from [89].

1.2 Mechanical properties of nanostructures similar to diatoms

Other studies of the mechanical properties of brittle materials under extreme geometric confinement, in particular nanowires, revealed that by decreasing the cross-sectional diameter, the material becomes stronger and is capable of undergoing significantly larger deformation before breaking [69, 49, 20]. The size scale effect on the Young's modulus of silica wires is shown in Figure 1-5. Experimental studies on silica nanowires of widths ranging from 230-800 nm revealed that fracture stress was influenced by specimen size, however, the modulus was not affected by size [66].

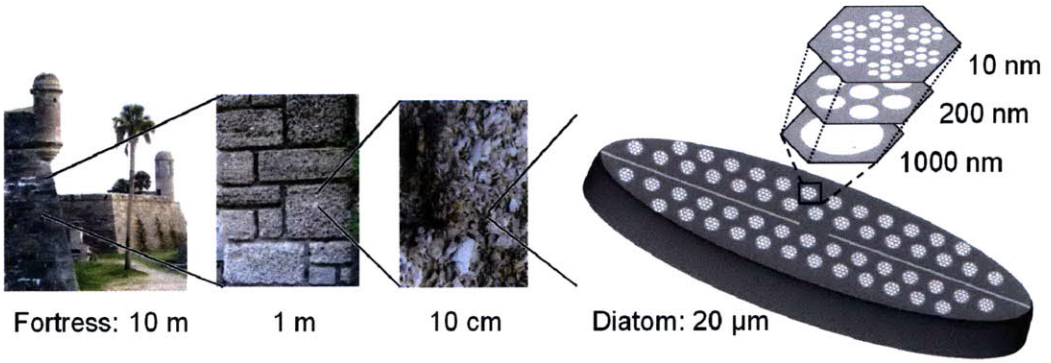

Figure 1-2: Merger of structure and material in engineering design [14]. The coquina stone found in this fortress, located in St. Augustine, FL, is extremely resilient in absorbing impacts such that cannon balls sink into, rather than shatter or puncture, attesting to its overall ductile response even though its constituents were made of brittle materials.

This study also determined that the modulus stayed constant at around 68 GPa, whereas the fracture stress varied from 8.77 to 6.35 GPa for the smallest and largest SiO_2 wire widths, respectively. Ni *et al.* [67] experimentally determined that modulus was independent of diameter for amorphous silica nanowires ranging from 50 to 100 nm in diameter. On the other hand, Silva *et al.* [80] found increasing stiffness for lower diameters by performing molecular dynamics (MD) simulations on amorphous silica nanowires. The fracture toughness of bulk vitreous silica was determined to be approximately 0.8 MPa $m^{1/2}$ [61]. The failure mechanisms occurring within the process zone at the crack tip in amorphous silica glass was studied by Bonamy *et al.* [8]. By implementing AFM experiments and MD simulations, the authors found that nucleation and growth of cavities are the dominant mechanism for failure within the process zone. Integrated silicon circuits have been manufactured with a wavy structural layout and 1.7 μm thickness, and can be elongated up to 10% [48]. Other studies revealed highly ductile amorphous silica nanowires, by using a taper-drawing process. Ranging from 20 nm in diameter and with highly smooth surfaces, the nanowires achieve extreme flexibility such that rope-like twists and spiral coils are realized [55]. However, even though these synthetic nanostructures offer attractive mechanical properties, they are generally unfeasible for mass production due to

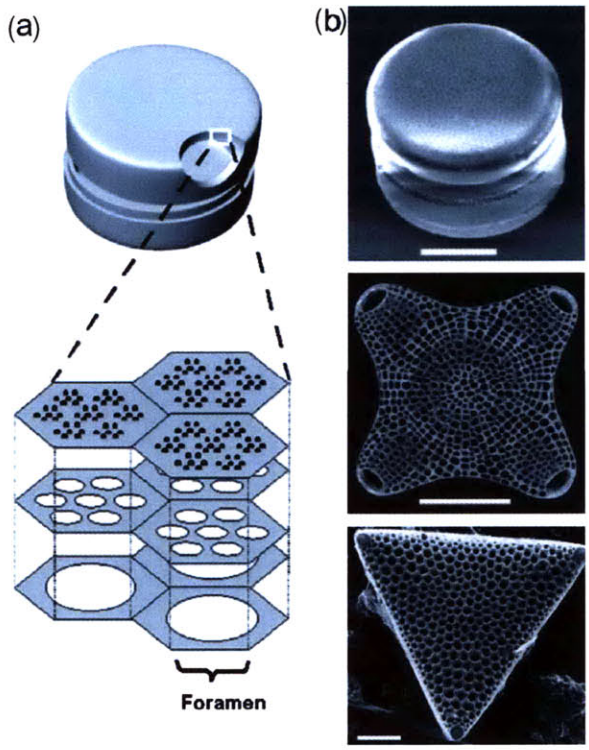

Figure 1-3: Hierarchical structure of diatoms, showing their porous silica structure. Panel (a): Schematic of the centric diatom frustule, showing the three porous silica layers lying along a hexagonal grid. Panel (b) shows AFM and SEM images of various diatom species, revealing their porous structural makeup. Scale bar: 10 μm. Images reprinted from [58].

complex and expensive manufacturing. For this reason, a second look at harnessing biomineralization is necessary. The first steps have already been taken by genetic sequencing of certain diatoms, allowing a better understanding at what proteins are responsible for the intricate nanoscale shapes seen on the frustules [5]. As the ability to create these magnificent structures increases, so does the necessity to understand the fundamental mechanical properties they endow. In light of this, we focus on a range of mineralized nanostructures found in diatoms and use atomistic simulations to probe the mechanical response and failure mechanisms. We hypothesize that the nanoporous geometry of the frustules is the key to providing enhanced toughness, ductility, and strength even though the constituting material itself is inherently brittle. Thereby, the formation of a nanostructured geometry that includes thin, geometrically confined structures of brittle elements may play a crucial role in understanding

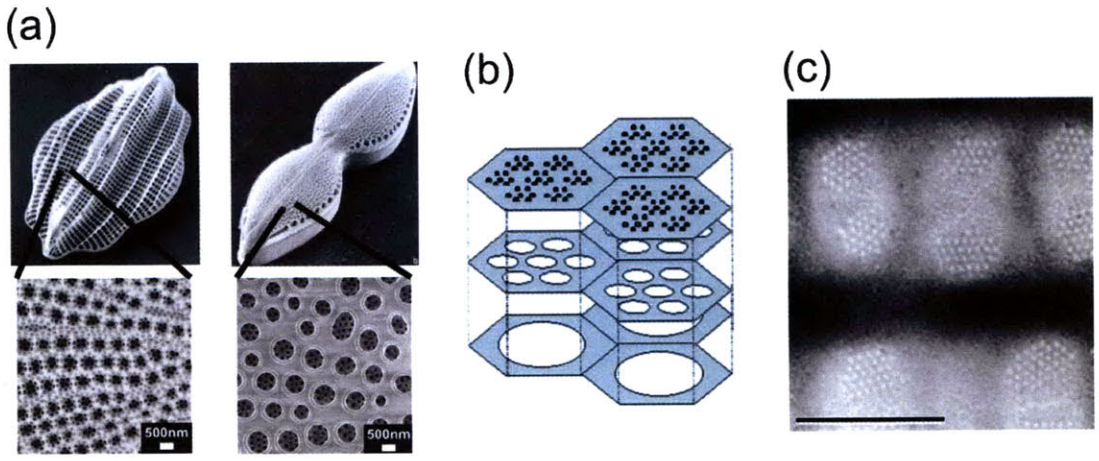

Figure 1-4: Hierarchical structure of diatoms, showing their porous silica structure. The SEM images in (a) show various diatom species, displaying the intricate hierarchical porous silica wall structure of diatoms. Panel (b) shows a schematic of the hierarchical structure. Panel (c) shows nanoscale voids observed in diatom algae, which are occluded by delicate a silicate membrane, called a hymen (*pl. hymens*), which is perforated by round pores (scale bar 200 nm). Images in (a) reprinted from [52]. Image in (b) reprinted reference [58]. Image in (c) reprinted from [62].

the materials behavior.

1.3 Outline

This thesis focuses on the mechanical properties of nanoscale structures found in diatoms. Within this context, size and shape effects are studied for silica and silicon systems. Indeed, diatoms are renowned for their mastery of living in harsh, mechanically extreme environments such as waterfalls and in strong sea currents. In Chapter 2, atomistic simulation methods are outlined and particular focus on the reactive force field, ReaxFF is presented. Chapter 3 focuses on the size dependence of the mechanical properties of nano silicon mesh structures, similar to those found in diatoms. Chapter 4 reveals the effect on the mechanical response and deformation mechanisms from adding two levels of hierarchy implemented in nanoscale silica, foils and meshes made up of interlocking foils, as found in diatoms. This chapter also focuses on the effect of hydration of nano silica structures and its mechanical response. In Chapter 5, geometric effects of amplitude and width on the mechanical response and defor-

mation mechanisms are obtained for folded nano silica structures, similar to those found in the diatom Ellerbeckia arenaria. Finally, Chapter 6 provides an overview of the fundamental importance and impact of biomineralized structures and its future applications while emphasizing prospective research.

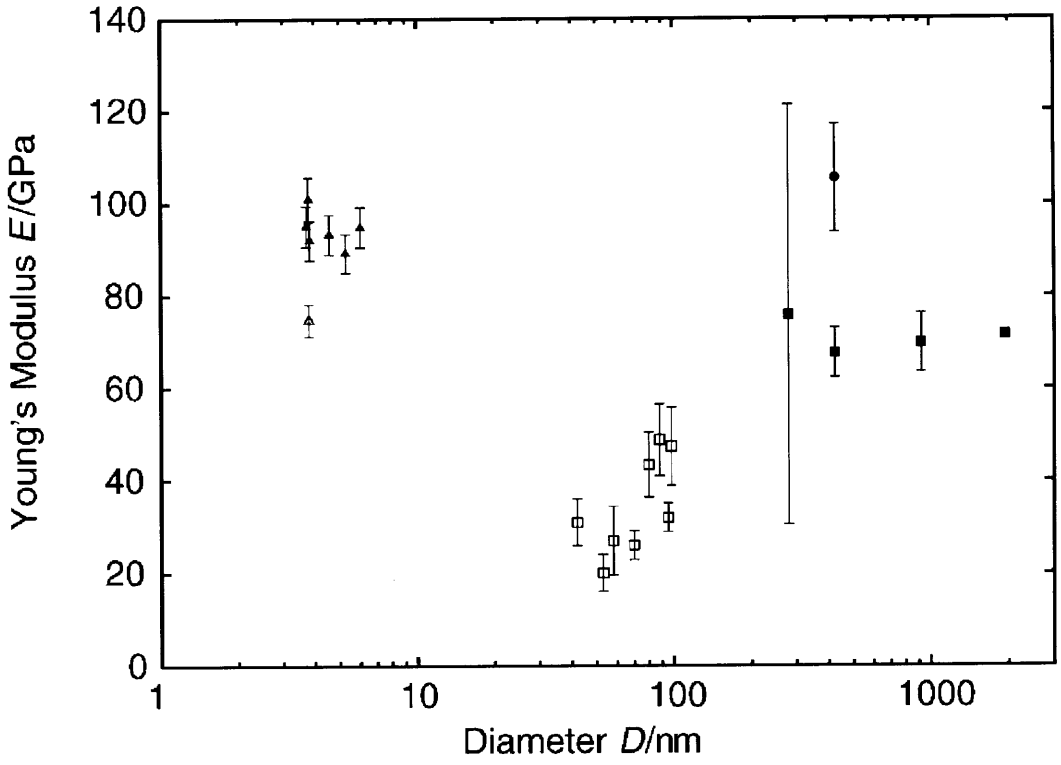

Figure 1-5: The size scale effect is a common phenomenon that influences mechanical properties at the nanoscale. The graph shows the Young's modulus of silica wires versus diameter, for different techniques: vertical experiments (■), in-plane experiment (•), resonant frequency experiments (□) [88, 21], MD simulations of nanowires and thin films (▲), and MD simulation of bulk silica (△). Figure reprinted from [80].

Chapter 2

Methodology

In this Chapter, an overview of atomistic simulations, and the reactive force field, ReaxFF is provided. A historical context illuminates the evolution of the atomic theory, with an overview of the models and simulation techniques. A description of the theoretical framework, applications, and limitations are given.

2.1 Atomistic modeling

The inception of the atomic theory dates back to approximately 400 B.C., with the Greek scholars Democritus and Leukippus, stating that the universe is made up of empty space and indivisible particles, or atoms [82]. They captured a compelling description, mentioning [42]: "Atoms, divergent in form, propel themselves through their separation from the infinite, into the great vacuum by means of their mutual resistance and a tremulous, swinging motion. Here gathered, they form one vortex where, by dashing together and revolving round in all sorts of ways, the like are separated off with the like."

Indeed this represents a striking resemblance to the actual behavior of atoms in regards to their motion, attraction, and repulsion. With this description as a harbinger to the more complex atomistic models of the twentieth century, it was not until 1957 that the first molecular dynamics (MD) simulation was published [3]. The fundamental principles of molecular dynamics are illustrated in Figure 2-1. Each atom is

simplified to a point representation, with trajectories in conjunction with the interactions between other atoms through interatomic potentials. By incorporating the Newtonian equation of motion, $F = ma$, and thermodynamic parameters, a description of the atom's position $\mathbf{r}(t)$, velocity $\mathbf{v}(t)$, and acceleration $\mathbf{a}(t)$ are gained.

Molecular dynamics offers a powerful elucidation of atomistic phenomenon, and in many respects allows for pioneering advances in understanding nanoscale material properties, deformation mechanisms, and even biological processes. In retrospect, the ability to describe atomic interactions has evolved in part thanks to a symbiotic relationship with computational technology. As the dawn of the computer age set forth with the mass production of the Universal Automatic Computer (UNIVAC) in the 1950's, MD studies would enter a new era. For example, the first MD simulation in 1957 [3], studied the phase transformation of a 32 particle system, proceeding at about 300 collisions per hour on the UNIVAC. The amazing development of computational processing currently allows the simulation of millions of atoms with near quantum detail [65]. An illustration of computing power advances relative to time is shown in Figure 2-2.

Within MD, the trajectories of the atoms are generated by applying ensembles such as Microcanonical (NVE) and Canonical (NVT) [7]. In the NVE ensemble, the number of moles, volume, and energy are constant. The exchange between the kinetic and potential energies describes the path of the atoms. In the NVT ensemble, the number of moles, volume, and temperature are constant. The energy created by straining the material is removed with a Berendsen thermostat. The Berendsen thermostat allows the velocities of the atoms to rescale towards the desired temperature of 300 K. The velocity Verlet algorithm is used to update the velocity of the atoms. The flowchart in Figure 2-3 lists the main steps comprising molecular dynamics simulations.

2.1.1 Mechanical analysis

We calculate the virial stress [94] by

$$\sigma_{IJ} = \frac{\sum_k^N m_k v_{k_I} v_{k_j}}{V} + \frac{\sum_k^N r_{k_I} \cdot f_{k_J}}{V}, \tag{2.1}$$

where I and $J = x,y,z$; and N, m, v, r, f, and V are the are the number of atoms, mass of atom, velocity, position, force, and total system volume respectively.

The engineering strain is defined as:

$$\varepsilon = \frac{\Delta L_y}{L_y}, \tag{2.2}$$

where L_y is the initial length of the specimen, and ΔL_y is the change in the length along the deformation direction (which is the y-coordinate). The stress-strain curve is then used to determine the elastic modulus, E, where $\sigma = \sigma_{22}$ (tensile stress in the loading direction):

$$E = \frac{\partial \sigma}{\partial \varepsilon} \approx \frac{\Delta \sigma}{\Delta \varepsilon}. \tag{2.3}$$

Once the stress-strain curves are determined, their integral is taken in order to determine the toughness:

$$E_V = \int_0^{\varepsilon_f} \sigma(\varepsilon)\, d\varepsilon, \tag{2.4}$$

where E_V, and ε_f are the energy per unit volume and strain at failure, respectively. A higher toughness indicates a greater ability of the material to absorb energy due to stresses before failure (resulting for instance in a larger fracture process zone). The Von Mises stress σ_v is calculated as

$$\sigma_v = \sqrt{\frac{(\sigma_{xx} - \sigma_{yy})^2 + (\sigma_{yy} - \sigma_{zz})^2 + (\sigma_{xx} - \sigma_{zz})^2 + 6(\sigma_{xy}^2 + \sigma_{yz}^2 + \sigma_{zx}^2)}{2}}, \tag{2.5}$$

where σ_{II} $(I = x, y, z)$ are the normal components of the stress tensor, and σ_{xy}, σ_{yz} and σ_{zx} are the shear components of the stress tensor. We apply the above expression (eq. (2.5)) for the Von Mises stress in plotting the atomic stresses throughout the

loading event.

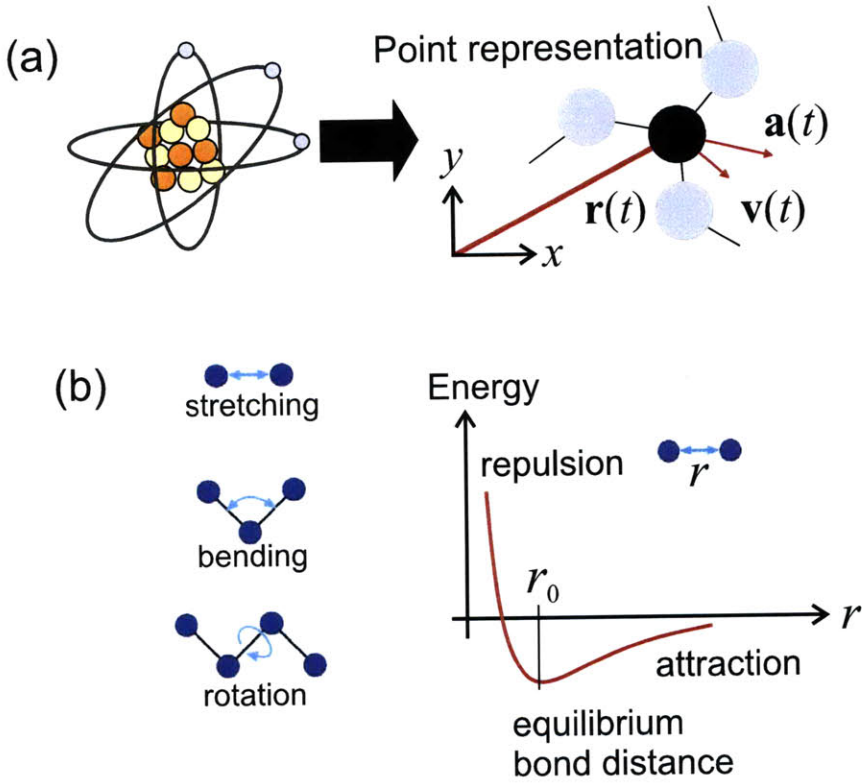

Figure 2-1: Molecular dynamics description. Panel (a): Atoms are represented as points that have a certain position, velocity, and acceleration. Panel (b): Each atom has an energy landscape and different bond terms, such as stretching, bending, and rotation between that atoms. Figure reprinted from [11].

2.2 Reactive Force Field: ReaxFF

Over the past decades, molecular simulation tools have taken various flavors, as shown in Figure 2-4. Many incorporate MD schemes with various types of potentials such as Tersoff-Brenner. At the heart of MD are potential energy functions (*i.e.* empirical force field (EFF) [25, 23] which depend on the location of the atoms and their respective energy contributions. The bond interactions can be described as springs (*i.e.* simple harmonic equations) that describe the compression and stretching of bonds and the bending of bond angles. The non-bonded interactions are described by van der Waals potential functions and Coulomb interactions. The potential functions

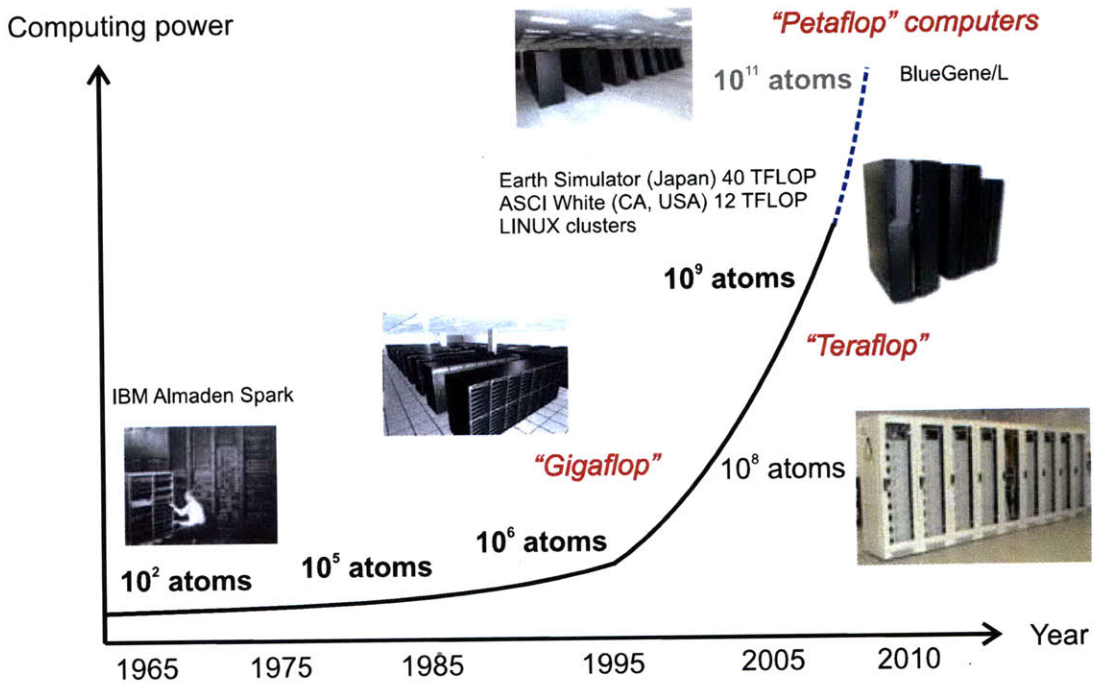

Figure 2-2: Computing power development and associated quantitative capacity to simulate atoms with simple interatomic potentials and short cutoffs. For more complex potentials, such as ReaxFF, significantly smaller number of atoms can be simulated. Figure reprinted from [13].

that are defined within EFF are fitted against experimental or quantum chemical data (*i.e.* training sets) [23]. The total system energy is separated into different energy contributions:

$$E_{system} = E_{bond}+E_{over}+E_{under}+E_{lp}+E_{val}+E_{pen}+E_{tors}+E_{conj}+E_{vdWaals}+E_{Coulomb} \quad (2.6)$$

Since the force field is empirically defined, it should only be applied to systems similar to the training sets [23, 87]. Reactive chemical systems are not properly defined by EFF methods since the shape of the potential function that defines the bond length/bond energy relationship makes it difficult to accurately determine a parameter value near the dissociation limit [23]. For instance REBO, the EFF method developed by Brener, allows the dynamic simulation of reactions in systems greater than 100 atoms. Nevertheless, REBO is limited because it excludes non-bond interactions and is based on a relatively small training set [23].

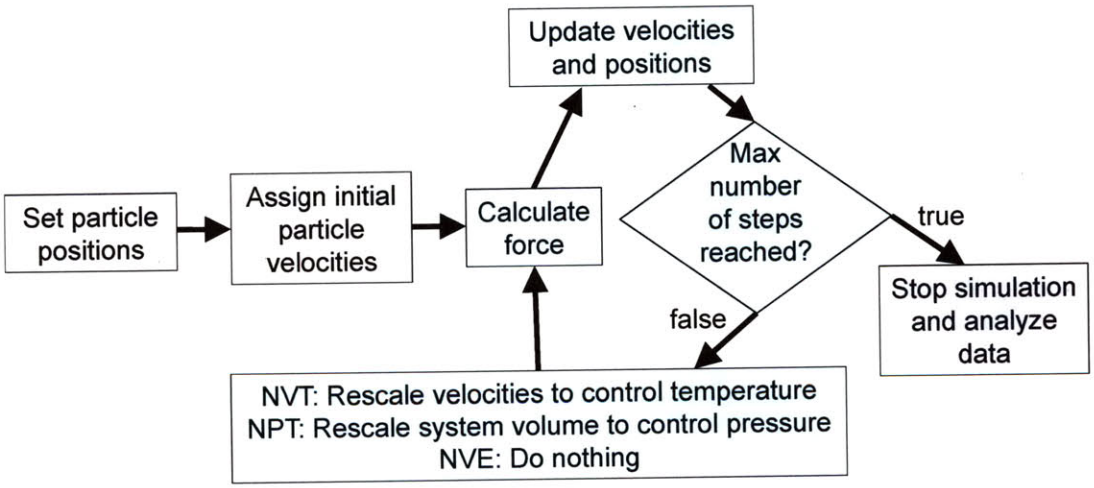

Figure 2-3: Flow chart showing the general methodology of molecular dynamics.

The development of ReaxFF [24] reactive force field offers a more accurate view of complex chemical systems (specifically for systems undergoing large strain or hyperelasticity) and therefore offers an alternative to the Tersoff-type potentials. ReaxFF is founded on quantum mechanical (QM) principles, such as DFT, and defines the atomic interactions with QM accuracy [24]. ReaxFF has been shown to more accu-

rately describe the material behaviors (e.g. the bond breaking and formation process) of non metals (C, O, H, N), metals (Cu, Al, Mg, Ni, Pt), semiconductors (Si), mixed Si-O systems, silica-water interfaces [78, 24, 26, 83, 68, 10, 19, 18, 29], and biological materials [12]. This aspect is critical to describe the properties of materials under large deformation. The ab initio calculations are quite computationally expensive and thus limit ReaxFF to systems containing a few thousand atoms. The computational time required by ReaxFF is mostly determined by the complexity of the mathematical expressions and the necessity to perform a charge equilibration (QEq) at each iteration [72, 9]. As a comparison, ReaxFF is approximately several orders of magnitude faster than quantum mechanics based on first principles (ab initio) methods. However, ReaxFF is 20-100 times more expensive computationally than simple empirical force fields such as CHARMM, DREIDING, or covalent type Tersoff's potentials [9]. The basic idea behind ReaxFF is to modulate the bond properties (*i.e.* bond order, bond energy, and bond distance) and therefore properly dissociate the bonds to separated atoms [24]. The valence angle terms are bond-order dependent, thereby making their energy contributions disappear when bonds break. Upon bond dissociation, the bond terms all smoothly go to zero and therefore no energy discontinuities appear during the reaction [24]. ReaxFF also describes the non-bond interactions between atoms by incorporating Coulomb and van der Waals potentials. Indeed, ReaxFF serves as a link between QM and empirical force fields [12, 9].

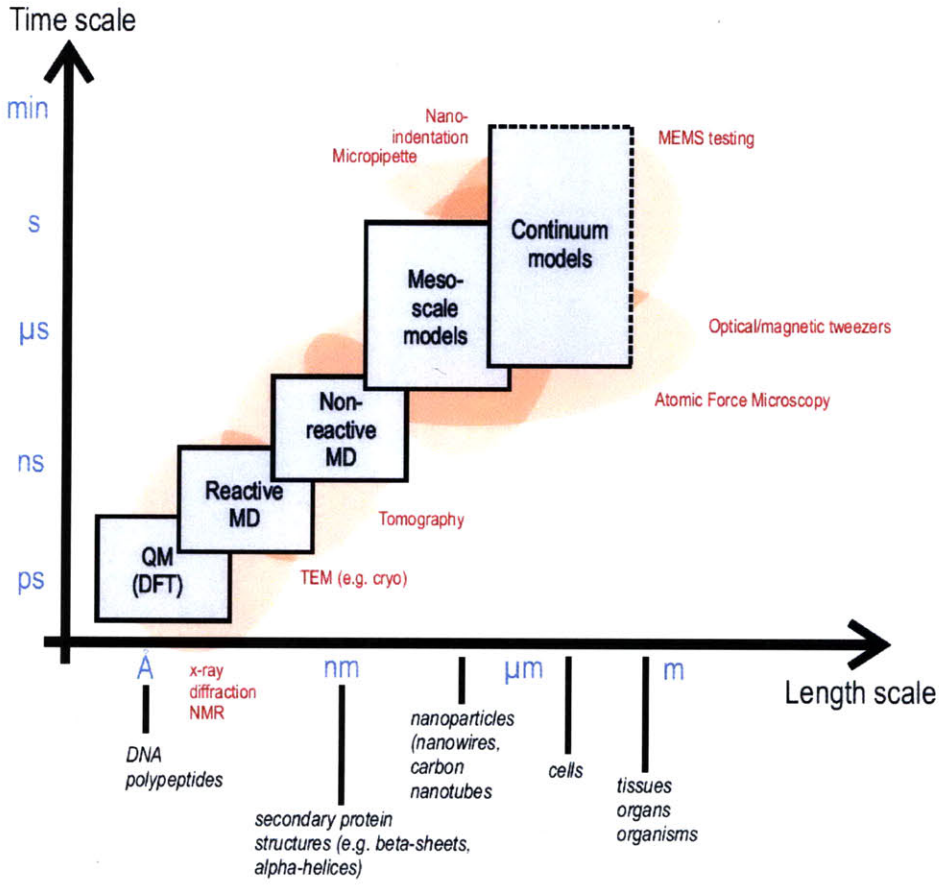

Figure 2-4: Time and length scales associated with different computational tools used in modeling materials. One important concept lies in the coupling of different computational and experimental tools which enable scaling up in terms of system size and time. For example, certain reactive molecular dynamics, such as ReaxFF, utilize principles derived from quantum mechanics and experiments. Continuum models reach the largest time and length scales, and can incorporate atomistic results. Experimental techniques, such as those in red font, enable the validation and provide data for different computational methods. In this thesis, the method used is ReaxFF, a type of reactive molecular dynamics. Figure reprinted from [16].

Chapter 3

Size dependence of the mechanical properties of nanoporous silicon structures

Indeed, diatoms are fascinating nanoscale structures that incorporate multiple engineering design concepts, perhaps resulting in an adaptation to improve their mechanical stability. We hypothesize that the nanoporous geometry of the frustules is the key to providing enhanced toughness even though the constituting material itself is inherently brittle. Thereby, the formation of a nanostructured geometry that includes thin, geometrically confined struts of brittle elements may play a crucial role in understanding the materials behavior.

Here we utilize the porous structure found in diatoms to develop a bioinspired nanoporous material implemented in silicon, as shown in Figure 3-1. The material consists of a porous structure with connected truss elements, where the width w of the nanotrusses is controlled in our analysis.We note that the goal of this study is not to develop a model that very closely reflects the specific structure of diatoms. Rather, our approach is guided by our desire to develop a general model system in which we can test the effect of the width of the nanotrusses on the bulk material behavior. The choice of silicon is motivated by the fact that a good interatomic potential, the first principles based reactive force field ReaxFF, is available for this material,

which has been validated against experimental results for mechanical properties, in particular large deformation and fracture of silicon [15, 10]. By varying the size of the constituting silicon nanostructure, we examine associated mechanical properties, as well as fracture and toughening mechanisms, facilitated through a series of molecular dynamics simulations in a computational materiomics framework [34].

3.1 Model geometry

We consider silicon crystals with uniform and ordered rectangular voids. All structures have an equivalent void length and height of 76 Å by 33 Å, respectively. The only parameter varied here is the wall width w, which ranges from 5 Å to 76 Å. Figure 3-1 shows the geometries considered here, representing different systems with variations of the wall width, w. The number of atoms varies between 672 to 15,232 from the smallest to the largest width systems. The simulation cell has dimensions of 217.20 Å x 152.039 Å x 10.86 Å in the x-, y- and z-direction.

3.2 Simulation approach

The structure is relaxed to its minimum potential energy and then loaded under tension along the [1 0 0] direction as shown in Figure 3-1(a), at a strain rate of 1×10^{10} s^{-1}. The system has periodic boundary conditions in all three directions, with a constant temperature of T=300 K controlled by the Nosé-Hoover thermostat. Deformation is applied by uniaxially increasing the size of the periodic simulation cell, while keeping all other dimensions of the simulation cell constant. Since the horizontal ligaments are interconnected with the vertical ones and because the poison effect along the non-loading directions are not considered, the stress state is globally multiaxial. We use a time step of 1 femtoseconds. The initial, unstrained silicon structure is shown in Figure 3-1(b). Aside from the variations in the geometry, all simulations are carried out under identical conditions, enabling us to perform a systematic comparison.

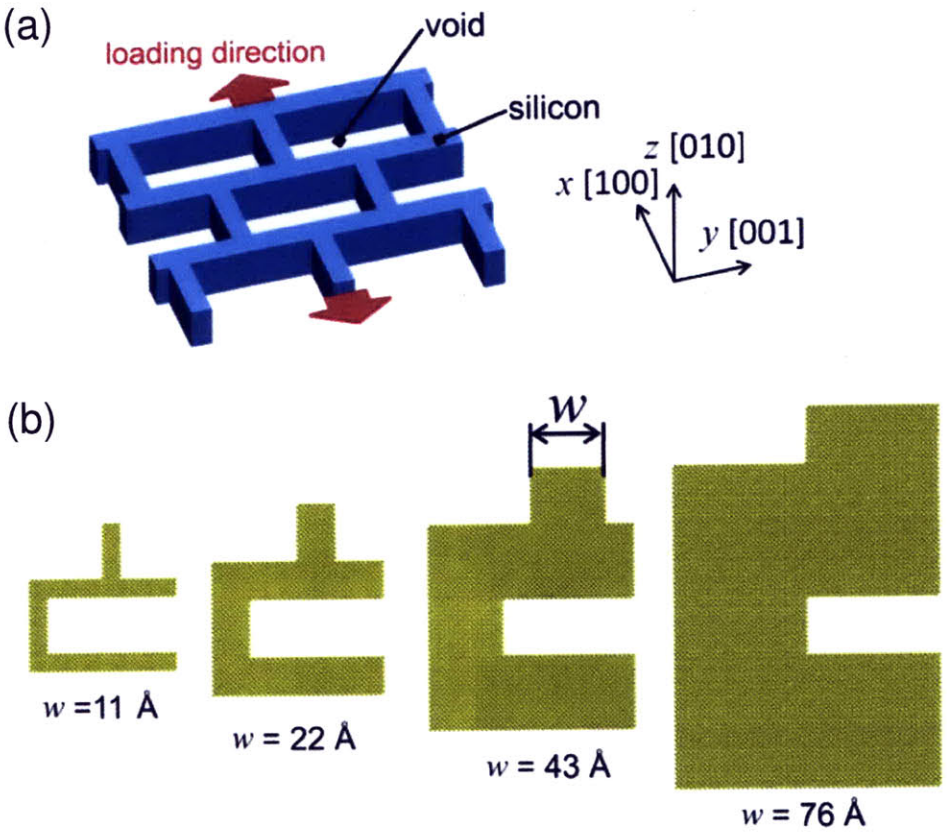

Figure 3-1: Geometry of the bioinspired silicon structure, and setup used in our simulations. Panel (a): Three-dimensional schematic of the silicon structure, with periodic boundaries along the x, y, and z directions. The arrows indicate tensile load applied uniformly along the structure. Panel (b): Initial geometry of structures considered here, illustrating the wall width (w, definition indicated in one of the structures) variation in the geometry.

3.3 Results and discussion

We now present a systematic analysis of the effect of changes of the wall width w on the resulting mechanical behavior (see Figure 3-1 for geometry). Figure 3-2 shows the stress-strain graphs for all sizes considered here, where the wall widths range from w = 5 Å to 76 Å. For smaller wall widths, we find that a greater plastic regime, lower maximum stress, and a lower modulus. Conversely, for larger wall widths we find a reduced plastic regime, larger maximum stress, and a higher modulus. The behavior of the material at larger wall widths more closely resembles that of bulk silicon, which is inherently brittle. However, due to lowering the wall width of the structure it is possible to dramatically change the behavior of the material towards a more ductile fashion, and facilitate the occurrence of very large deformation up to 80% without breaking. We ascribe the decrease in the maximum stress and the modulus with lower wall widths from free surface effects and a change of the stress distribution in the sample. Furthermore, the prominence of the plastic regime found for decreasing wall widths is not solely a phenomena caused by surface effects, but one that is augmented by the nanoscale porous architecture, which allows for a conformational change from a rectangular to hexagonal shape due to the change in the stress state, becoming more uniform as the wall width decreases.

We proceed with an analysis of the stress fields and the structural changes of the nanostructure during deformation of the material. Figure 3-3 shows the Von Mises stress field in the elastic regime, at 7% strain, for different wall widths. It can be recognized that for smaller wall widths, the stress is more homogeneously distributed throughout the system, and that a greater fraction of the atoms feature a higher stress level. In larger systems, the formation of a stress concentration at the corners can be recognized, suggesting a possible point for the nucleation of cracking or shearing. Figure 3-4 shows the Von Mises stress field at the maximum stress, for different wall widths. Here the strain value at which the snapshot was taken changes for the different cases considered (see stress-strain graphs shown in Figure 3-2), and the relevant strain level is indicated in the plot. For widths smaller than 11 Å, the structure at

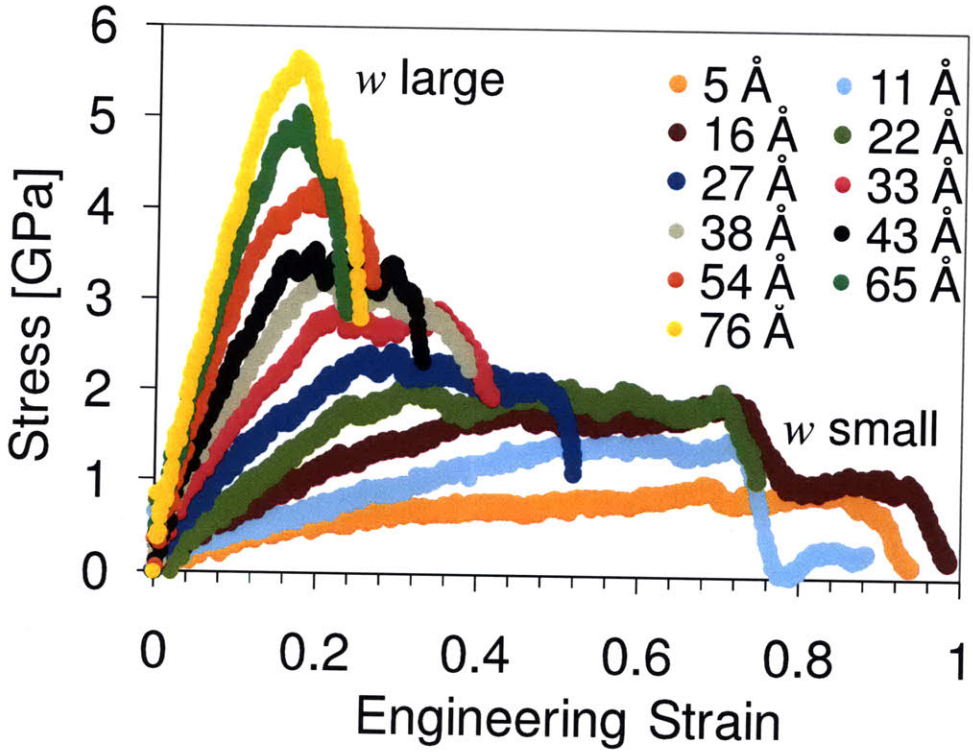

Figure 3-2: Stress-strain graph for all sizes. Wall widths range from $w = 5$ Å to 76 Å. For smaller wall widths, there is a greater plastic regime, lower maximum stress, and lower modulus. Thus, due to the lowering of the wall width of the structure (w), the system behaves in a more ductile fashion and sustains very large deformation up to 80%.

the maximum stress becomes hexagonal at the maximum stress, representing a significant structural transformation compared with the initial rectangular structure. It is evident that the stress is distributed homogeneously throughout the structure. For larger wall widths, high stresses are concentrated around the corners and in diagonally oriented regions in the sample. Moreover, the initial, rectangular shape of the structure is maintained up to the maximum stress, suggesting a limited capacity of the system to undergo plastic deformation. Indeed, further analysis at larger strains (during the failure process) confirm this conjecture. Figure 3-5 depicts the Von Mises stress field during failure for different wall widths, where again the strain value at which the snapshot was taken is indicated in the plot. For the systems with wall widths of 11 Å and 22 Å, necking and formation of beaded molecular structure is observed, quite similar to what has been seen in earlier studies of metal nanowires. At widths of 43Å and larger, we observe that nanocracks initiate from the corners and then arrest, leading to further necking. Shear deformation in these thinned parts of the structure contributes to the final failure of the samples. For widths of 76 Å and similarly large systems we observe the formation of voids within the sample along the plane of shear. The shearing direction is orientated at roughly 45° degrees with respect to the tensile direction. Failure mechanisms in silicon nanowires examined in earlier molecular dynamics and experimental studies show similar results as observed in our simulations, in that the fracture process zone undergoes amorphization [40, 44]. In our simulations, the region surrounding the failed region tends to be amorphous. We estimate that the amount of amorphization (determined from the edge where failure takes place) extends at most 10-15 Å into the sample. Crack arrest is due to the nanoscale geometry, and can also be explained by simultaneous cracking. For example, for the 43 Å wall width, both cracks initiate on the same ligament but on opposite edges. One crack travels through the vertical ligament (which is the dominant crack), while the other crack travels into the adjacent horizontal ligament at roughly 45° degrees to the loading plane. The crack that travels perpendicularly through the vertical ligament has less distance to traverse, and thus passes through the ligament before the other crack can. Therefore, the 45° degree crack arrests since the system

is no longer intact. For slower strain rates of 1×10^{9} s^{-1}, the crack arrest mechanism still occurs, but wedge which is formed from the nondominant crack is smaller than those from 1×10^{10} s^{-1}.

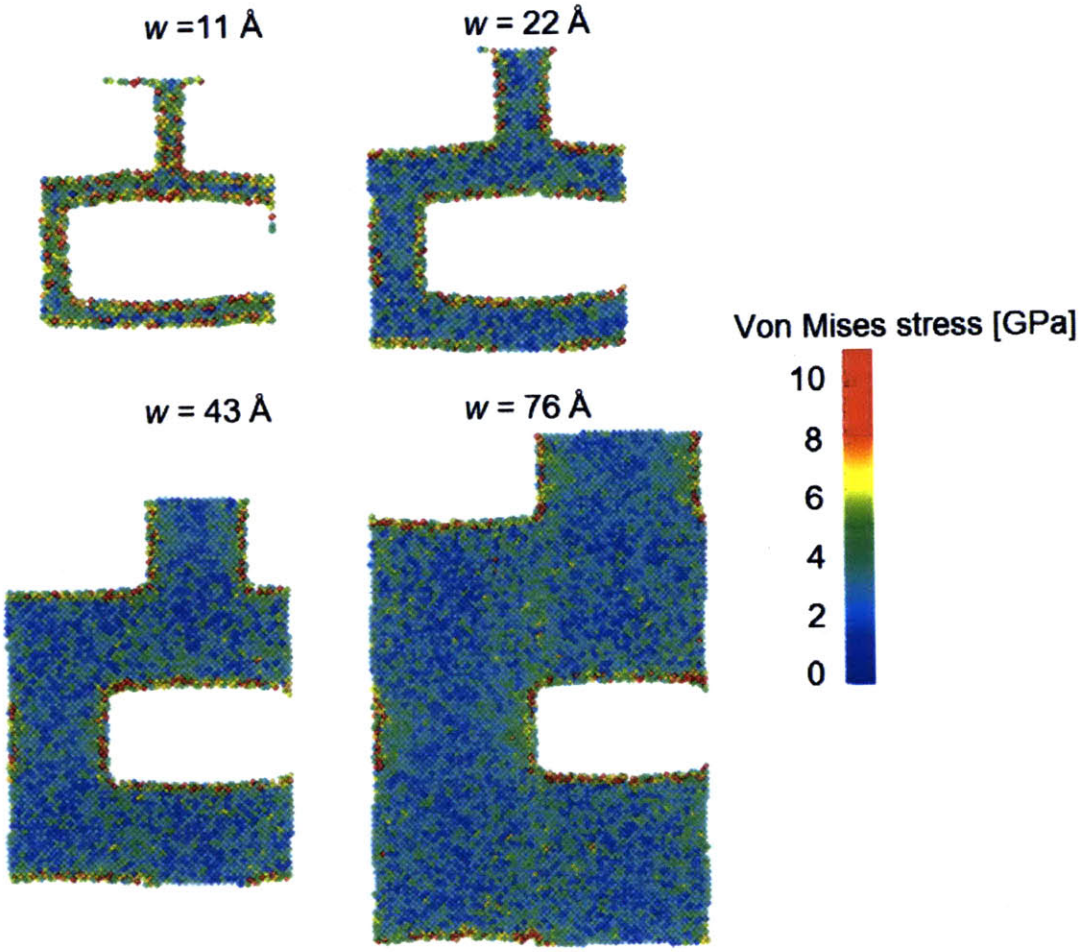

Figure 3-3: Von Mises stress field in the elastic regime, at 7% strain, for different wall widths. For smaller wall widths, the stress is more homogeneously distributed throughout the system, and a greater fraction of atoms have higher stress. In larger systems, a stress concentration at the corners can be recognized.

The analysis reviewed above suggests that the change in wall width induces a change in the stress distribution during deformation. This is confirmed with an analysis of histogram plots of the Von Mises stress, as shown in Figure 3-6, where results are shown for $w = 11$ Å and 76 Å. Figure 3-6(a) depicts the results at the maximum stress. For $w = 11$ Å the stress distribution shows a peak at a larger stress than at $w = 76$ Å. Figure 3-6(b) depicts the results during failure. It is found

that the stress distribution in the w = 76 Å case is much different from the one in the w =11 Å case. For w = 11 Å, the stress distribution shows a peak at a much larger stress (6.5 GPa) compared with a peak at w = 76 Å (2.8 GPa) along with a broader tail. The broader tail in the large system indicates a more heterogeneous distribution of the stress in the sample. Finally, in Figure 3-7 we summarize the effect of wall width variations on various mechanical parameters. Figure 3-7(a) plots the variation of the plastic regime, Figure 3-7(b) the toughness, Figure 3-7(c) the maximum stress, and Figure 3-7(d) the elastic modulus. Both the maximum stress and modulus are found to increase with the wall width. A general trend of larger plastic regimes for decreasing wall widths is observed as well, reaching plastic regimes approaching 40% for the smallest systems considered with a wall width of a fraction of a nanometer. For wall widths larger than 27 Å, the toughness plateaus at around at 9×10^8 J/m^3. Between 16 Å and 27 Å a sharp increase in toughness is observed, with a maximum at 16 Å. Below 16 A, the toughness drops to around 7×10^8 J/m^3, denoting an inverse trend. The reason for the greater variation in toughness for w = 27 Å are fluctuations in the initial deformation mechanism from necking to crack formation, perhaps due to the fact that this system is close to the critical dimension between the transition between the two types of extreme behavior. The results depicted in Figure 3-7 clearly show that by controlling the wall width, a significant improvement of the material performance can be achieved. Specifically, at a critical dimension of 18 Å, the material features the greatest possible toughness. Overall, the study shows that the bioinspired silicon nanoporous bulk material provides great toughness at great deformability.

3.4 Conclusion

By employing an atomistic simulation method derived from first principles quantum mechanics, we have examined the deformation and failure behavior of bioinspired porous silicon structures as shown in Figure 3-1. The inspiration for the structural design is based on porous silica cell walls of diatoms, unicellular algae that boast an

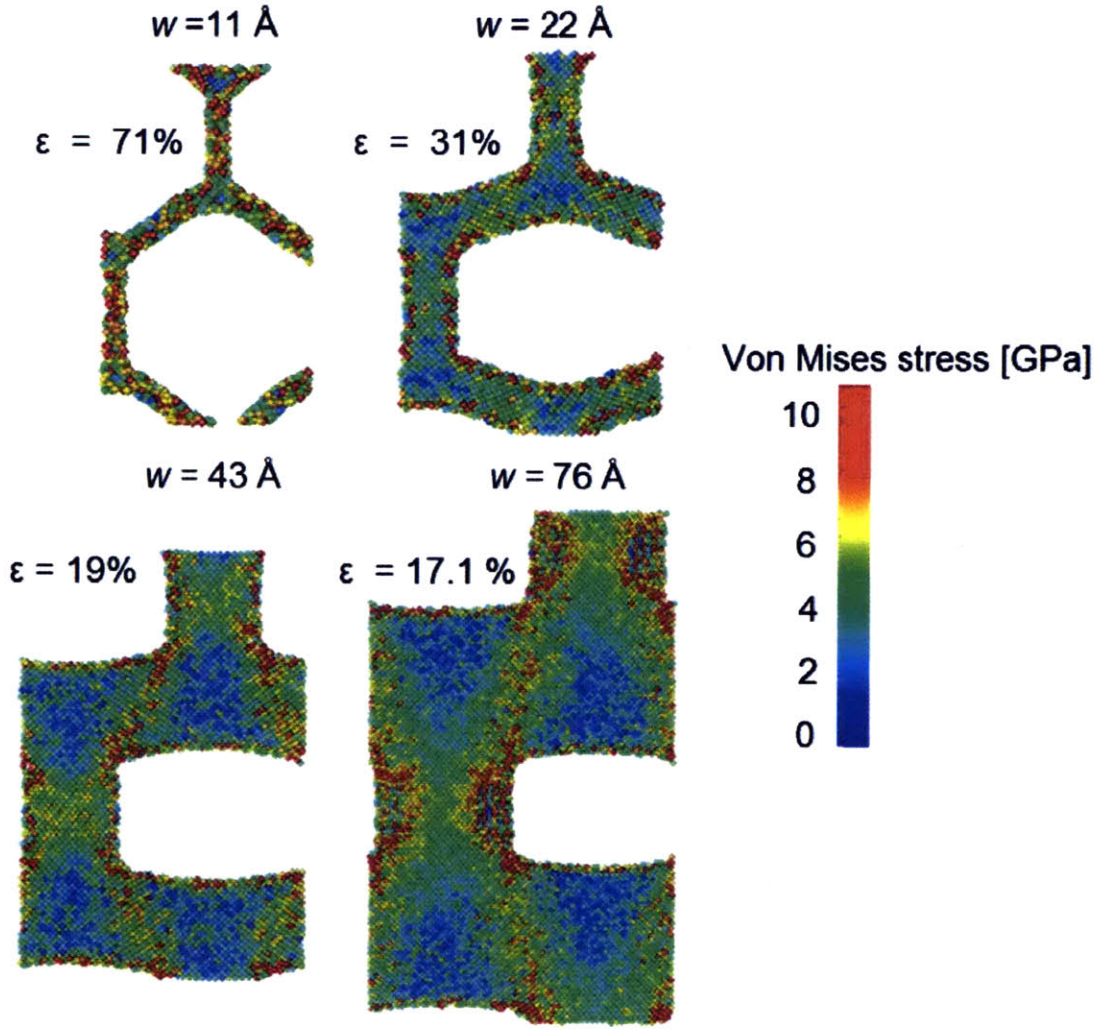

Figure 3-4: Von Mises stress field at the maximum stress, for different wall widths (the strain value at which the snapshot was taken is indicated in the plot). For widths smaller than $\approx$ 11 Å, the structure at the maximum stress becomes hexagonal, and the stress is distributed homogeneously throughout the structure. For larger wall widths, high stresses are concentrated around the corners and in diagonally shaped regions in the sample. Moreover, the initial, rectangular shape of the structure is maintained.

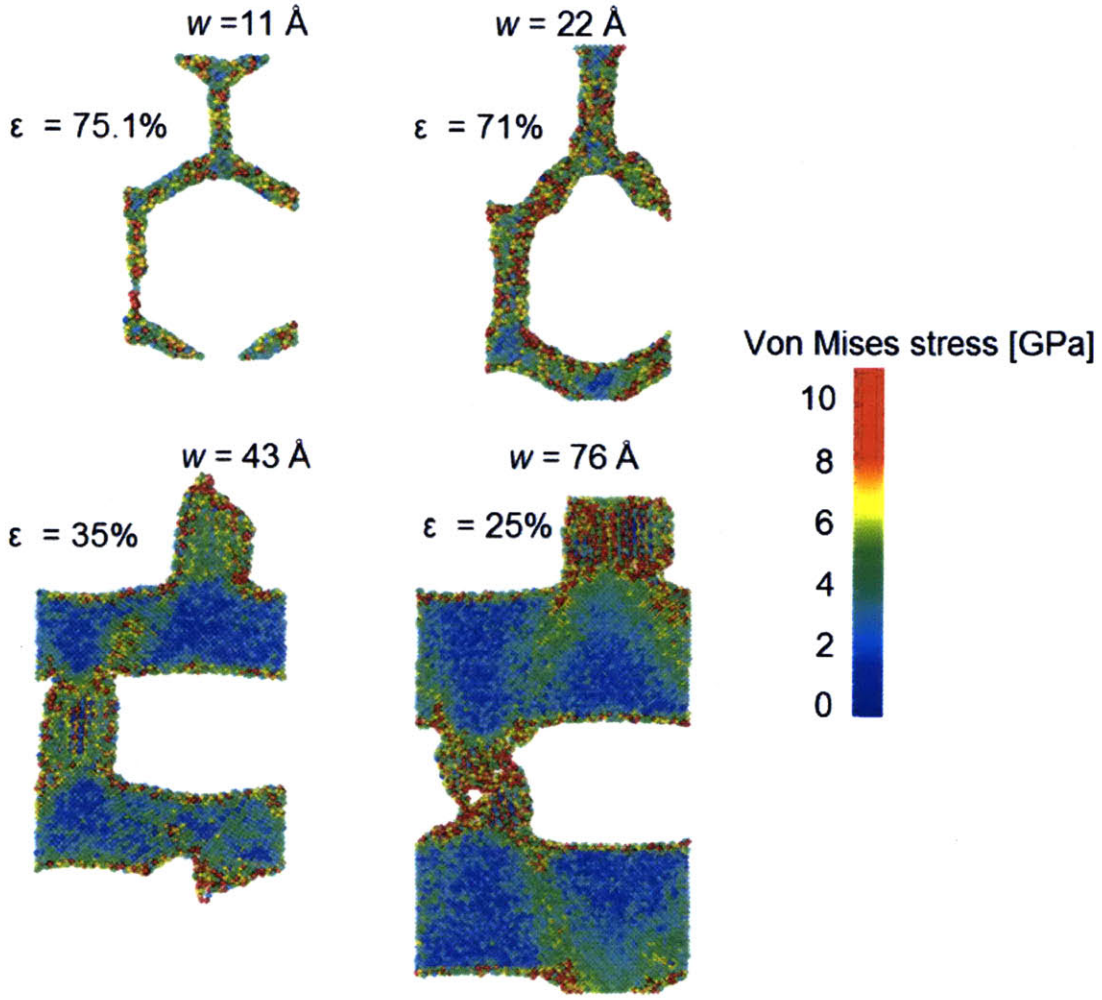

Figure 3-5: Von Mises stress field during failure for different wall widths (the strain value at which the snapshot was taken is indicated in the plot). For the systems with wall widths of 11 Å and 22 Å, necking and formation of beaded molecular structure is observed. At widths of 43 Å and larger, cracks initiate from the corners and then arrest, leading to further necking. Shear deformation in these thinned parts of the structure contributes to the final failure of the samples. For widths of 76 Å and similarly large systems we observe the formation of voids within the sample, where the region surrounding the failed region is amorphous. The failure mechanism remains similar for the wall widths below 43 Å, and is characterized by a structural change from a rectangular to hexagonal shape. An analogy to plastic hinges can be drawn to describe the mechanism for allowing large deformation. For larger systems, however, the failure mode is consistently crack propagation, an effect that is confirmed to exist for varying strain rates.

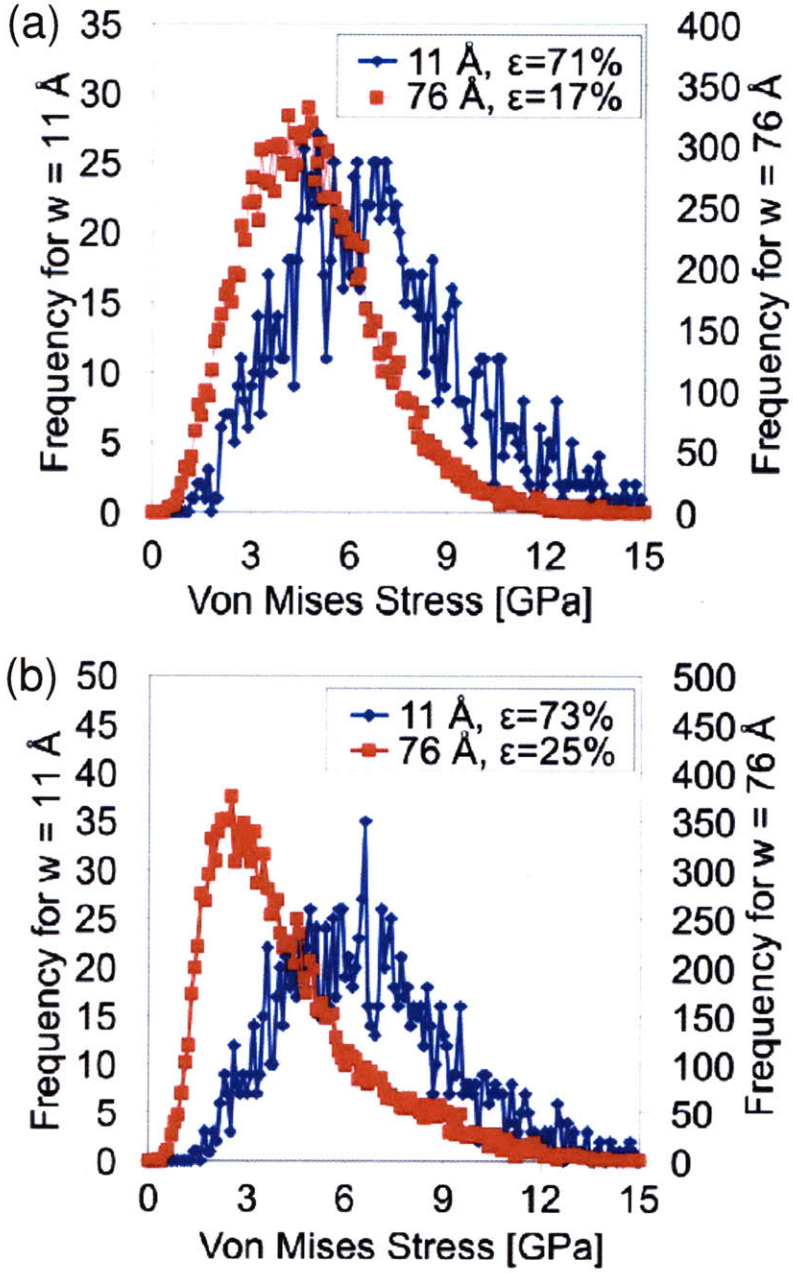

Figure 3-6: Histogram plots of the Von Mises stress, (a) for $w = 11$ Å and 76 Å (at the maximum stress), and (b) for $w = 11$ Å and 76 Å during failure. Panel (a): For $w = 11$ Å the stress distribution shows a peak at a larger stress than at $w = 76$ Å. Panel (b): During failure, the stress distribution in the $w = 76$ Å case is much different from the one in the $w = 11$ Å case. For $w = 11$ Å, the stress distribution shows a peak at a much larger stress ($\approx$ 6.5 GPa) compared with a peak at $w = 76$ Å ($\approx$ 2.8 GPa) along with a broader tail. The broader tail in the large system indicates a more heterogeneous distribution of stresses.

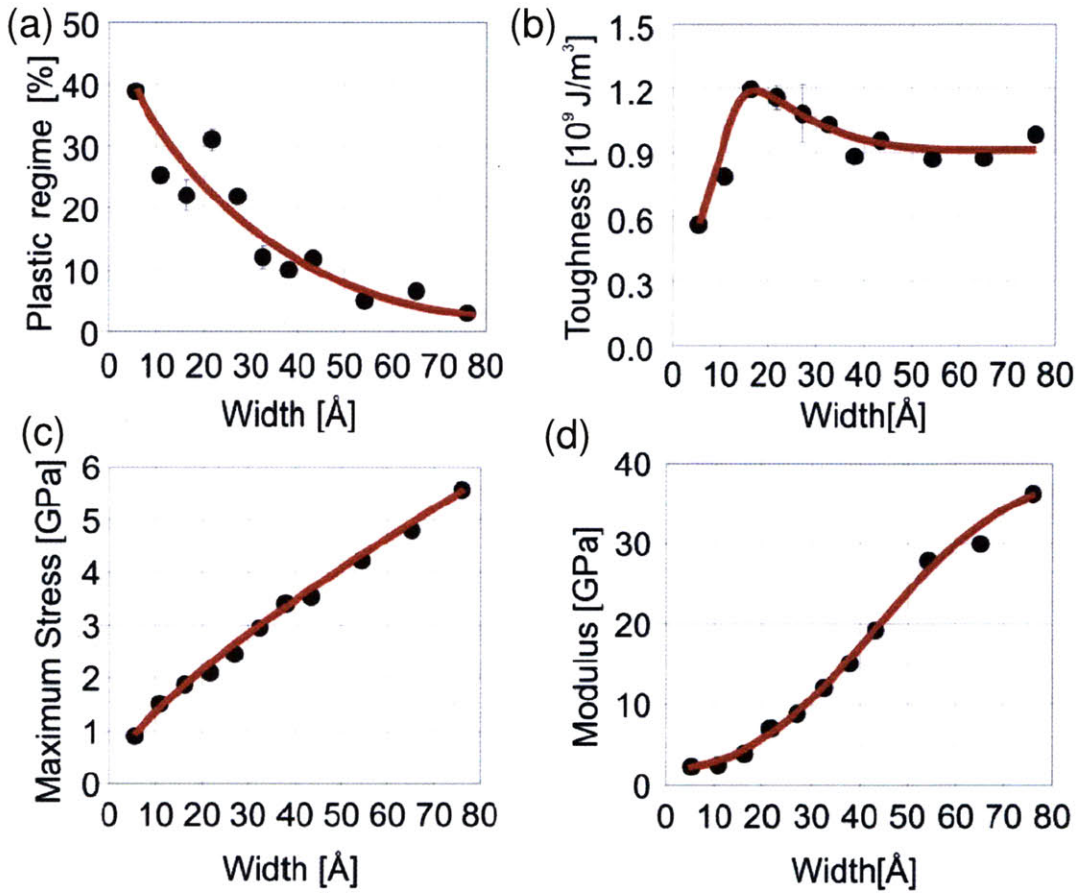

Figure 3-7: Effect of wall width on (a) the plastic regime, (b) toughness, (c) maximum stress, and (d) elastic modulus. Both the maximum stress and modulus are found to increase quasi-linearly with the wall width. A general trend of a higher plastic regime for decreasing wall width is observed as well. The plastic regime is estimated by measuring the length of the linear plateau region which is associated with constant stress. For wall widths larger than 27 Å, the toughness plateaus at around at 9×10^8 J/m^3. Between 16 Å and 27 Å a sharp increase in toughness is observed, with a maximum at $\approx$ 16 Å. Below 16 Å, the toughness drops to around 7×10^8 J/m^3, denoting an inverse trend. The error bars are determined by dividing the standard deviation by the square root of simulation runs (that is, the standard error of the mean (SEM)). All simulations were repeated four times. For graphs (c) and (d), the error bars are smaller than the data points surrounding it so they cannot be identified in the plot.

intriguing hierarchical design and interesting mechanical properties (Figure 1-3).

Through carrying out a systematic analysis, we have captured the variation in mechanical properties, as summarized in Figure 3-7. Through the design of a nanoporous structure with ultra-thin trusses, the material response of silicon has been altered from brittle to highly ductile, where the most ductile systems with wall widths below 1 nm feature a plastic regime of almost 40%, and a modulus of 2.3 GPa. The most brittle responses are observed for the systems with the largest wall width, with a vanishing plastic regime, albeit a larger modulus of more than 30 GPa. We find that an important aspect in promoting the ductile response of the material is the ability to alter the initial rectangular shape into a hexagonal one, which occurs for $w <$ 33 Å. Interestingly, a Hall-Petch and inverse Hall-Petch like effect was observed for the toughness; with a maximum toughness of 1.2×10^9 J/m^3 corresponding to $w =$ 16 Å (see, Figure 3-7(b)). In comparison, the toughness values of high-performing engineering bulk amorphous materials range from 10 to 100 $\times10^6$ J/m^3 for ceramics and 10×10^6 J/m^3 for Ti alloys [45]. Plain lightweight aggregate concrete and steel fiber reinforced concrete has a compressive toughness of 150×10^3 J/m^3 and 290×10^3 J/m^3, respectively [46]. In light of these toughness values, the material considered here shows a manifold increase of the toughness.

The knowledge derived from the simulations reported here heralds a paradigm shift in the design of conventionally brittle materials by showing that its mechanical response can by greatly altered by simple alteration of its structural geometry at the nanoscale without the need to introduce new constituents. This merger of material and structure is a powerful concept that could provide new ideas for a broader class of bioinspired materials with advanced properties. Specifically, our study provides a strategy to transform an inherently brittle material towards a very ductile one, illustrating how a weakness is turned into a strength simply by controlling its structure. This is achieved by providing large elasticity and plasticity by adding ordered nanopores to a brittle system, where the underlying mechanism change is due to surface effects and a change in the stress distribution. The deformation mechanism, incorporating structural changes in the organization of the material in the bulk sys-

tem, is unique and does not strictly resemble that of one-dimensional nanowires. The overarching feature of diatom shell structures is their nanoscale porosity, which we use here as a template in finding mechanical properties of similar structures. We achieve this by applying the ordered nanoporous design concept found in diatoms shells in developing a new silicon nanomaterials where key design features are transferred. Such a material could have many applications in the development of structural materials, filters, optical materials, and many others. For the fabrication of the class of materials discussed here, self-assembly techniques could be used, for example based on protein, peptide or other molecular scaffolds [1, 91]. A similar strategy is found in the synthesis of diatoms, providing a possible path to manufacturing these materials with great precision to reach relevant length-scales [75, 43]. The great abundance of brittle materials in nature – such as silica or other minerals, combined with novel energy efficient self-assembly techniques, could provide a new route for the development of lightweight, strong and tough materials with small ecological footprint.

The studies reported here have focused solely on variations of the wall widths, and does not address other design parameters such as the aspect ratio or the overall geometry of the nanostructure. Further analysis of other geometric variables may thus be another promising avenue of future work and could provide additional insight in optimizing the material. It may also be interesting to incorporate topology optimization to tailor certain mechanical properties. In the next chapter, a detailed analysis of the mechanical properties and advantages of hierarchical structures representative of diatom frustules is established.

Chapter 4

Size and hierarchy dependence of the mechanical properties of nanoporous silica structures

As diatom structures are relatively complex, reaching multiple degrees of hierarchy and size, revealing the intricate interplay between structure and mechanical response requires delicate and systematic analysis. The previous chapter established a framework on size effects on the mechanical response of silicon mesh structures. In order to understand the diatom's mechanical properties more fully, we now examine hierarchical silica structures, a common feature observed in diatoms. The mechanical properties of diatoms are quite attractive, allowing for very high toughness, a quality that is indeed attributed to the complex hierarchical topology resembling honeycombs within honeycombs. In this chapter we study two structures resembling those of Figure 1-4 [33].

4.1 Model geometry

We consider a structural design composed of alpha-quartz crystals. One structure is a foil or infinitely tall thin wall, whereas the other is a mesh composed of interlocking silica foils thus forming uniform and ordered rectangular voids. Since the simulation

box is periodic, the foil structure can be thought of as a periodic array of thin foils with a spacing s equivalent to the mesh structure. Figure 4-1 shows the geometries considered here. Both the mesh and foil structures are exposed to free surfaces. The foil has free surfaces parallel to the y axis; and the mesh has free surfaces along the x and y axis.

All mesh structures have an equivalent void dimension of 76 Å by 30 Å. The only parameter varied here is the wall width w, which ranges from 5 Å to 72 Å for both foil and mesh (see Figure 4-1). The number of atoms varies from 750 to 17,000 for the smallest to the largest width silica systems. The largest simulation cell has dimensions of 151 Å × 196 Å × 8.5 Å in the x-, y- and z-direction. We performed a relaxation for 80 ps of a 31 Å foil structure with free surfaces along the x and y axis. It was found that there was negligible average stress after relaxation. This result could be explained since surface reconstruction does not take place.

4.2 Simulation approach

All structures are equilibrated under the canonical ensemble at 300 K for a time of 10 ps and then loaded under uniaxial strain loading along the [1 2 0] direction as shown in Figure 4-1(a), at a strain rate of 1×10^{10} s^{-1} at 300 K. The system has periodic boundary conditions in all three directions and the temperature is controlled by the Berendsen thermostat [7]. Deformation is applied by uniaxially increasing the size of the periodic simulation cell in the loading direction only, while keeping all other dimensions of the simulation cell constant. We use a time step of 0.2 femto-seconds. The initial, unstrained silica structure is shown in Figure 4-1(b). Aside from the variations in the geometry, all simulations are carried out under identical conditions, enabling us to perform a systematic comparison.

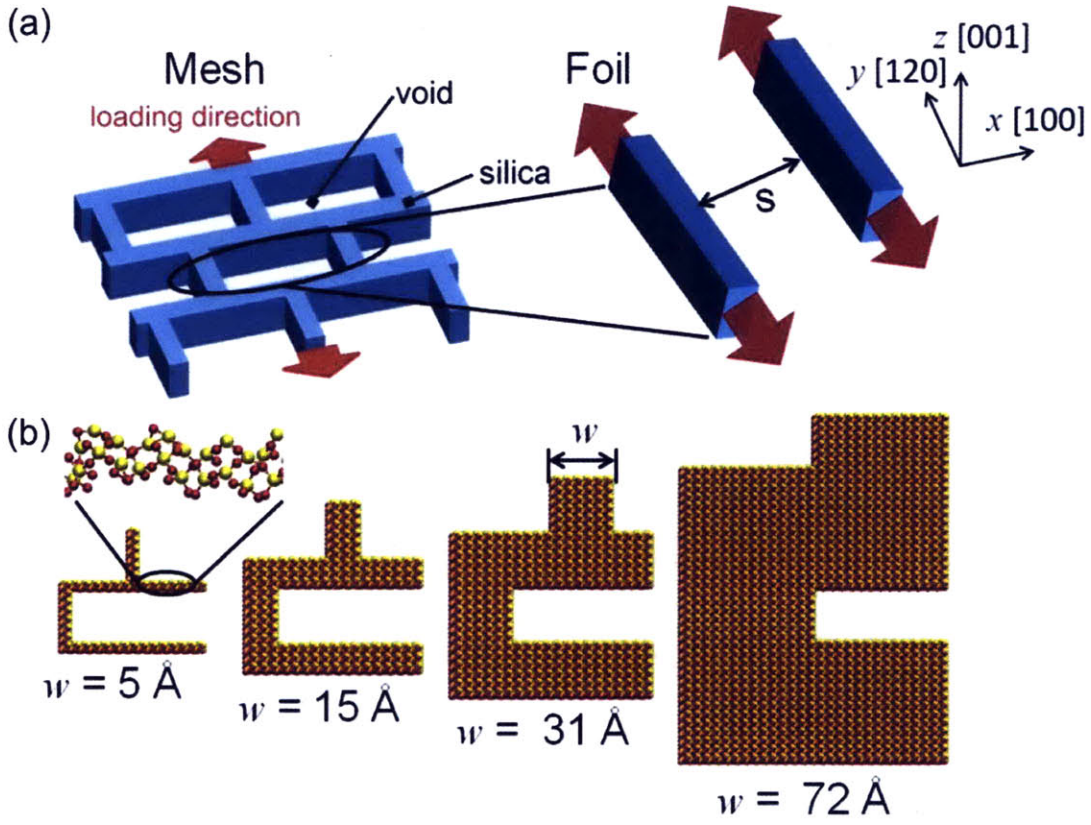

Figure 4-1: Geometry of the hierarchical bioinspired silica structure, and setup used in our simulations. Panel (a): Three-dimensional schematic of the silica mesh structure (shown on left), with periodic boundaries along the x, y, and z directions. On the right, the geometry of the silica foil array structure is shown, and has periodic boundaries along the z and y directions with free surfaces only along the x axis. The spacing s between the foils is equal to that in the corresponding mesh structure. The crystallographic orientation is the same for all silica structures considered. The lowest level of hierarchy represented here is the foil, and the highest is the mesh structure. The arrows indicate tensile load applied uniformly along the structure. Panel (b): Initial geometry of mesh structures considered here, illustrating the wall width (w, definition indicated in one of the structures) variation in the geometry. The inset shows a detailed view of the relaxed surface structure. Wall widths are similarly varied for the foil as in the mesh structure.

4.3 Results and discussion

We begin our analysis by focusing on the effect of changing the wall width on the mechanical properties of the two levels of hierarchy (see Figure 4-1(a) for the two geometries considered, that is, foil and mesh). As shown in Figure 4-1, the wall widths are varied between $w = 5$ Å to 72 Å for both the foil and mesh structures. From a structural hierarchy perspective to materials design, the first order of hierarchy consists of a foil oriented such that the only two free surfaces are in the x direction. The second order of hierarchy is composed of a mesh of interlocking foils with voids and free surfaces in both x and y directions. The z axis has no free surface, and thus the structure can be described as consisting of infinitely tall walls, or foils.

Figure 4-2(a) shows the stress-strain response of the foil structure for varying widths w, and Figure 4-2(b) shows the same data for the mesh geometry. Both the foil and mesh structures show an increase of deformation in the plastic regime, a lower modulus, and lower maximum stress with decreasing wall width w. However, the silica mesh structures have a much greater plastic regime than the silica foil. The first important observation made here is that even though silica is considered a brittle material, the results show that it is possible to transform it into a ductile system for small (nanoscale) wall widths, which reach a maximum failure strain of 90% and 120% for the silica foil and the mesh structure, respectively. In a similar fashion as the foil structures, the silica mesh also shows an increased modulus and maximum stress for larger wall widths. The plastic regime in the mesh structure decreases with increasing wall width, albeit showing a less severe drop than in the case of the foil structure. Interestingly, the maximum tensile stress is reached at roughly the same strain of 34% for the silica foil, for all $w \geq 15$ Å (see Figure 4-2).Another important difference between the foil and mesh structures lies in a gradual versus a sharp increase of elastic modulus for increasing wall width, respectively. Furthermore, the foil structures show a stiffening effect at widths $w > 15$ Å. Previous studies have also shown either stiffening or softening effects, which are affected by the orientation of the loading (since silica is anisotropic). For example, silica nanorods modeled

using the BKS and TTAM potentials showed a softening effect when under tension [93, 79]. Another study conducted *ab initio* simulations using the PAW method and found a pressure dependence on the bulk modulus of silica [50]. Experimental measurements of silver nanowires loaded in tension along the [0 1 1] direction found a stiffening behavior [90]. Copper nanowires also show either stiffening or softening, depending on the crystallographic orientation, as shown by earlier analyses using the EAM potential [54].

In order to gain a deeper understanding of the corresponding mechanisms that explain the size dependent behavior of the material, we now proceed to analyze the stress fields during deformation. We first turn to the failure mechanisms found in the silica foil structures displayed in Figure 4-3. We find that void formation occurs for $w > 15$ Å, and first nucleate near the surfaces. Subsequently, voids coalesce and grow, ultimately leading to fracture. The trajectory of void nucleation events occurs roughly on one plane inclined to the loading axis, and for the largest $w = 72$ Å structure, they bifurcate onto two planes, allowing for larger regions of void coalescence. In all silica foil structures, beading down to thin atomic chains is observed towards the end stages of failure before complete fracture is observed. Although no clear signs of dislocation or shear band nucleation are observed, the initial mechanisms of cavity nucleation are consistent with other molecular dynamics simulations and experimental studies of silica deformation [8, 76]. Previous studies on small diameter nanowires (similar in size to those in our study) have determined that the mechanism of yielding by dislocation is absent, and demonstrated that the main mechanical instability is a disorder-order transformation, resulting in the reduction in size of the nanowire neck until single atom chains emerge [49, 63].

We proceed with analysis of the silica meshes as shown in Figure 4-4, which shows the equivalent von Mises stress field at the maximum stress. For larger wall widths, high stress is mostly concentrated on the surface and specifically near the edges, thus suggesting possible locations for crack or shear nucleation. However, with lower wall widths, the stresses become relatively homogeneous throughout the structure. For large deformation, the void shapes gradually change from a rectangular to a

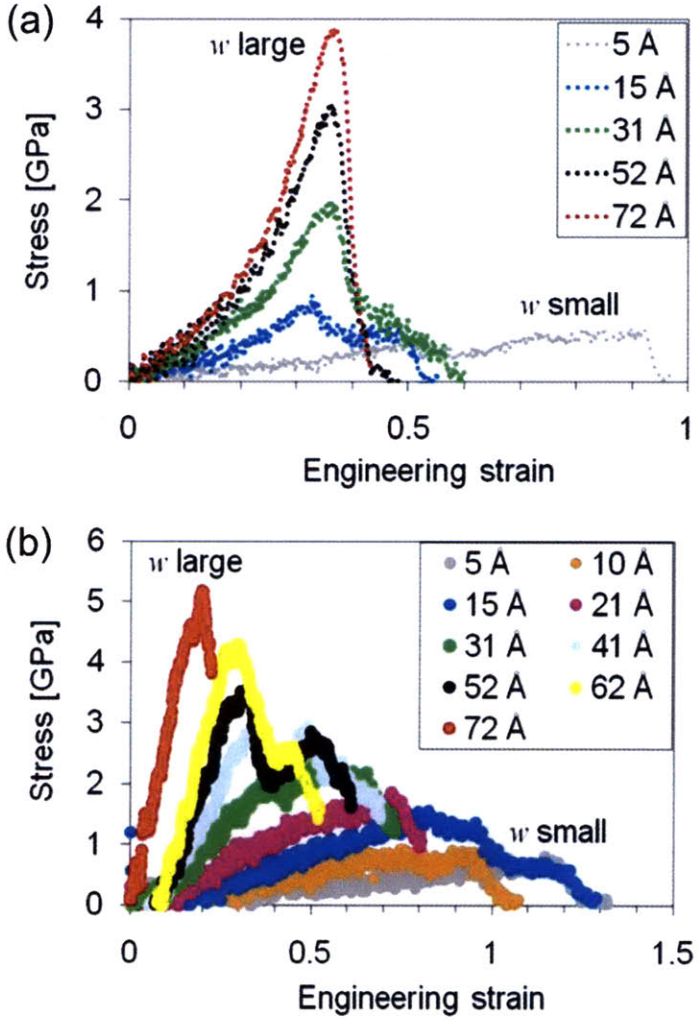

Figure 4-2: Stress-strain graph of silica foil (panel (a)) and mesh structure (panel (b)), for all sizes (wall widths range from $w = 5$ Å to 72 Å). Panel (a): For smaller wall widths, there is a greater plastic regime, lower maximum stress, and lower modulus. Thus, due to the lowering of the wall width of the structure (w), the system behaves in a more ductile fashion and sustains very large deformation up to 115%. The strain hardening region observed for $w = 52$ Å is due to a temporary crack arrest due to the stretching and shearing of a secondary horizontal ligament. The crack continues its path once the secondary ligament stops deforming. Panel (b): For wall widths above 15 Å, there exists a plastic regime of about 1% to 5%. The greatest deformation is obtained for the smallest wall width of 5 Å. Failure mechanisms are characterized by void formations near the center or edge of the foil which then coalesces with other voids until the structure is no longer intact. Cracks are not observed for the foil, whereas in some mesh structures, cracks occur. The reason for stiffening for wall widths > 15 Å is due to nonlinear elasticity within the core, along with a Poisson effect as seen in earlier studies.

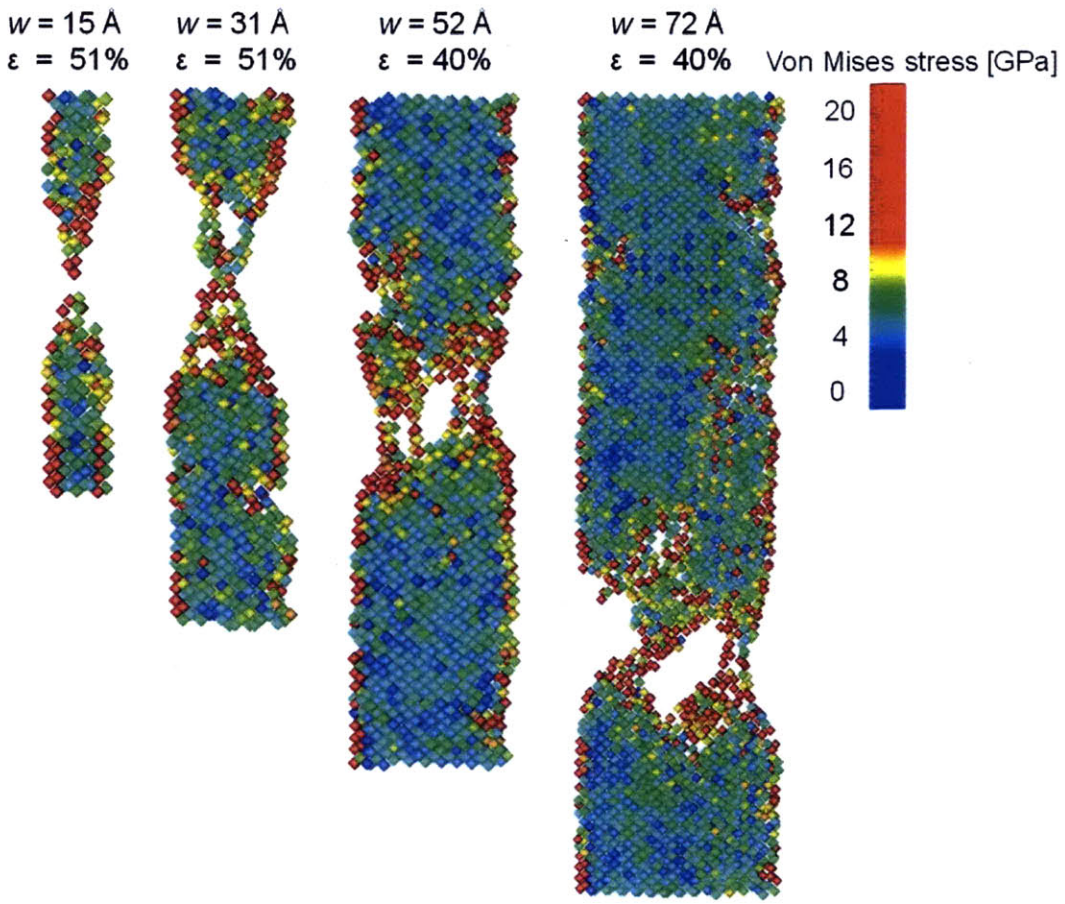

Figure 4-3: Von Mises stress field during failure, for different foil wall widths (the strain value at which the snapshot was taken is indicated in the plot). The Highest stresses are localized near the failure zones and the surface. The figure also reveals the deformation mechanisms, showing the locations of void nucleation and coalescence. Bifurcation of voided regions and shear like behavior is observed for $w = 72$ Å. A beading mechanism narrowing down to thin strings of atoms is observed for the final stage in deformation. In order to improve image clarity, we only show the stress values associated with silicon atoms when plotting the stress fields. Generally, the oxygen atoms have a much broader stress distribution than silicon atoms, and therefore the stress patterns are difficult to observe if both atom types are shown.

hexagonal one for decreasing wall widths, and can be clearly seen for $w \leq 31$ Å. High levels of shear stress also manifest in a diagonal pattern as shown in Figure 4-5 for $w > 31$ Å , which facilitate possible regions of void nucleation and the start of failure. Once crack failure starts, the stress is concentrated around the fracture process zone, as shown in Figure 4-6. The deformation mechanisms observed for varying wall widths are dramatic in that they correlate with the peaking of toughness, and can be summarized as follows. For $w > 62$ Å and $w < 21$ Å, the dominant failure mechanisms are brittle crack propagation, and beading down to thin atomic chains respectively. However, for 21 Å $\leq w \leq$ 62 Å, crack propagation and shear mechanisms occur in a competing fashion, and allow for increased toughness. For example, for $w = 52$ Å structure, we observe a crack arrest phenomenon and corresponding increase of tensile stress from 2 GPa to 2.8 GPa, which is due to shear mechanisms occurring within the junctions of the mesh elsewhere (see Figure 4-7).

The analysis discussed in the preceding paragraph explains the remarkable stress-strain response of mesh structures with thin wall widths, as shown in Figure 4-2(b). The key to explain these is the geometric pattern that allows large deformations to be accommodated by the mesh by changing from a rectangular pattern to a hexagonal one at large strains (see, e.g. in Figures 4-4 and 4-6), specifically for wall widths below 31 Å. The fundamental reason for these very large strains without failure is due to the more homogeneous distribution of stresses and the geometry transformation from rectangular to a hexagonal shape for smaller wall widths.

In Figure 4-8, we summarize the effect of wall width variations and hierarchy level on the mechanical properties – the plastic regime, toughness, maximum stress, and ductility. In all structures considered here, the plastic regime increases with decreasing w. The maximum stress and modulus both increase with the wall width, and the ductility increases for smaller wall widths. For the largest wall width in silica and silicon structures, the range of ductility is between 30 % to 50 %. The greatest ductility is observed for the silica mesh with smallest wall width of 5 Å, reaching 120%. The silica foil shows a gradual increase in modulus with width, with a maximum of 6.7 GPa for $w = 72$ Å, whereas the mesh structures sharply increase in

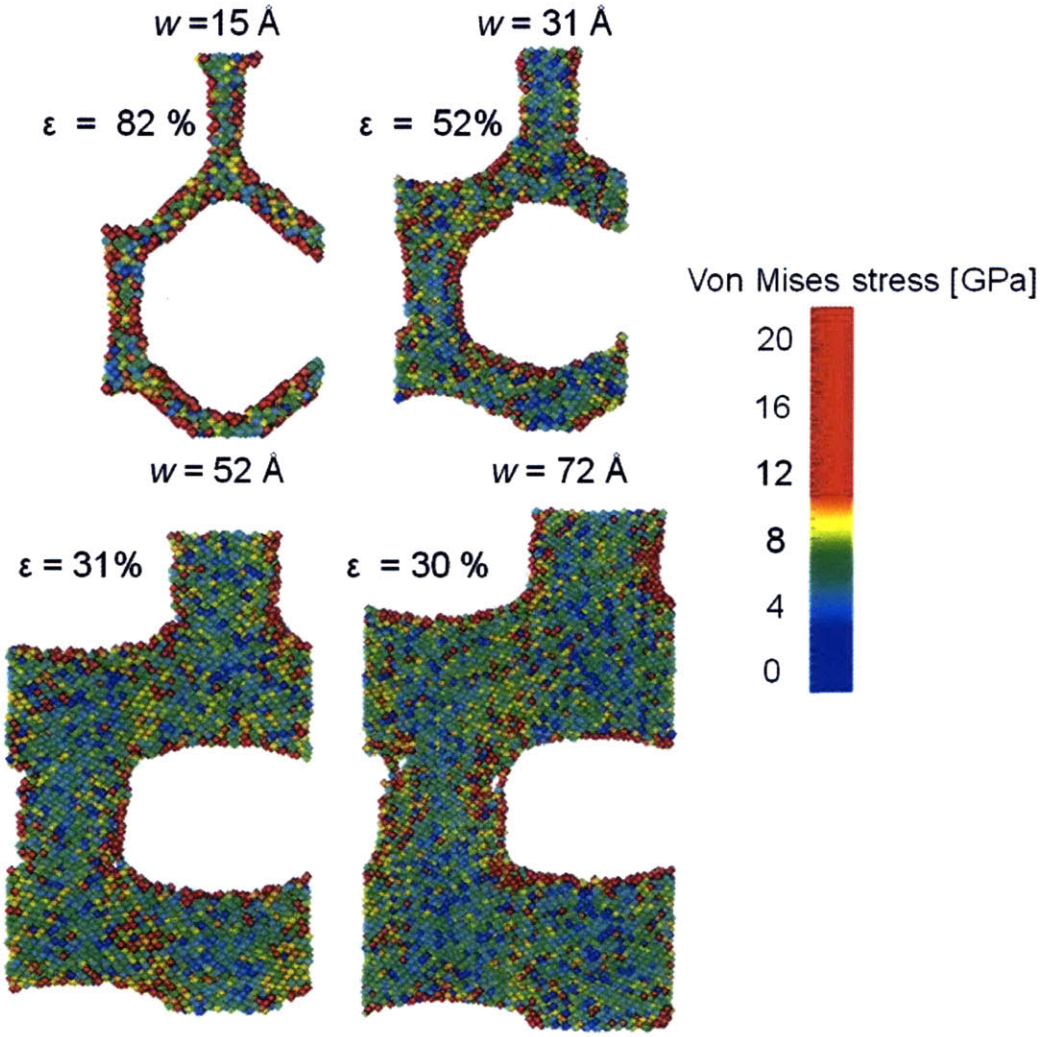

Figure 4-4: Von Mises stress field at the maximum stress, for different mesh wall widths (the strain value at which the snapshot was taken is indicated in the plot). For widths smaller than $\approx$ 31 Å, the structure at the maximum stress becomes hexagonal, and the stress is distributed homogeneously throughout the structure. For larger wall widths, high stresses are concentrated around the corners. Moreover, the initial, rectangular shape of the structure is maintained. In order to improve image clarity, we only show the stress values associated with silicon atoms within the silica system.

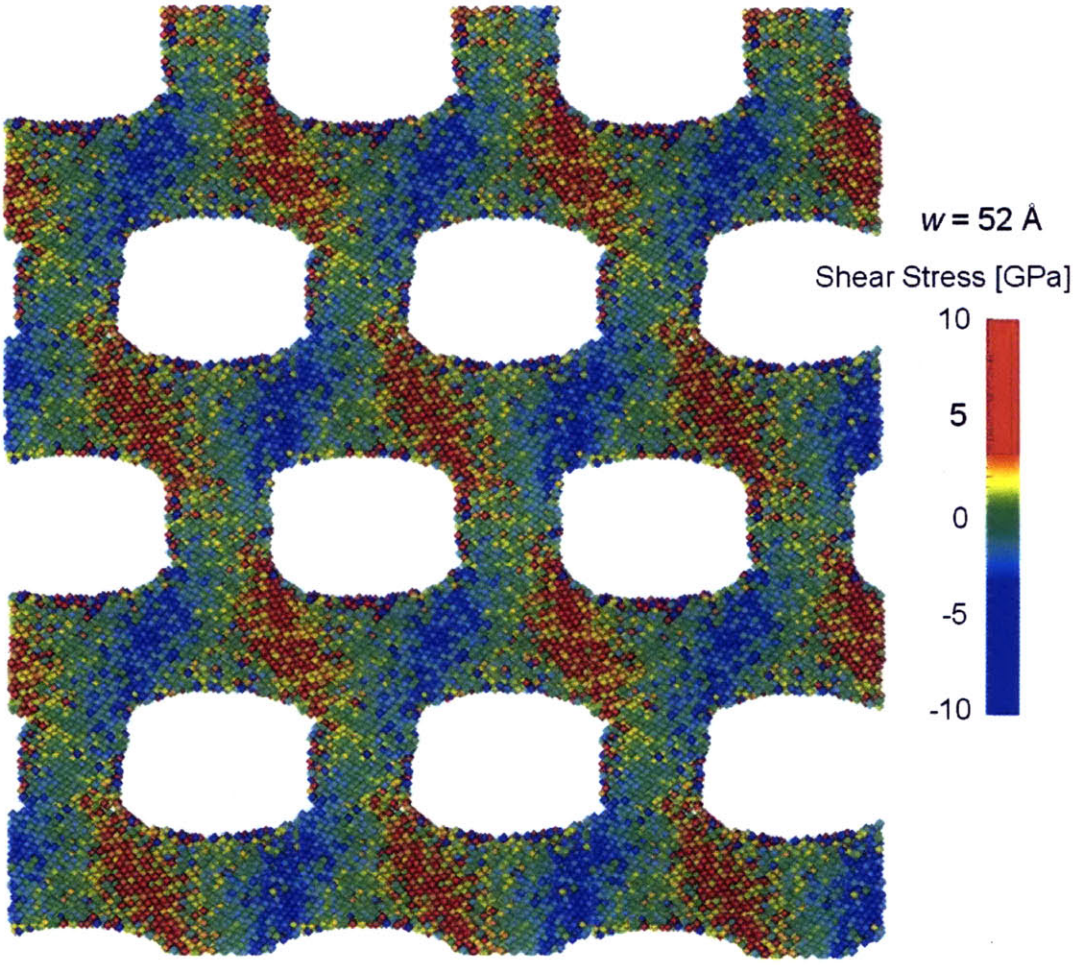

Figure 4-5: Shear stress σ_{xy} taken at maximum stress for the system with wall width $w =$ 52 Å. High regions of shear stress form a diagonal pattern and suggest possible areas where deformation occur. We show multiple sets of the periodic cell so that the stress pattern can be clearly seen. In order to improve image clarity, we only show the stress values associated with silicon atoms within the silica system.

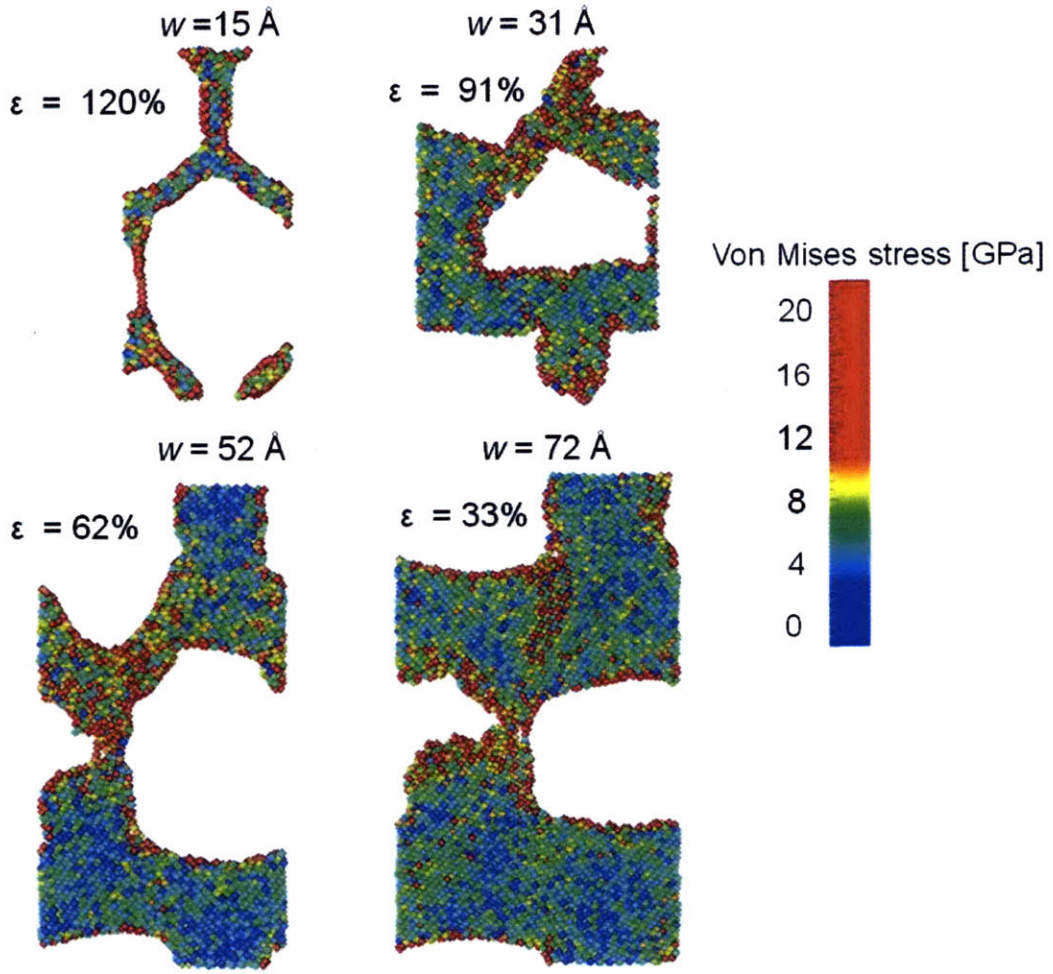

Figure 4-6: Von Mises stress field during failure for different mesh wall widths (the strain value at which the snapshot was taken is indicated in the plot). For the systems with wall widths of 15 Å and 31 Å, necking and formation of beaded molecular structure is observed. At widths of 52 Å and larger, cracks initiate form the corners. For $w \geq 31$ Å, we observe the formation of voids within the sample, specifically within the regions surrounding the failure process zone. The failure mechanism remains similar for $w \geq 52$ Å, and is characterized by a structural change from a rectangular to a hexagonal shape. An analogy to deformation in mascroscopic plastic hinges can be drawn to describe the mechanism for accommodating large deformations. For larger systems, however, the failure mode is consistently crack propagation, an effect that is confirmed to exist for varying strain rates. In order to improve image clarity, we only show the stress values associated with silicon atoms within the silica system.

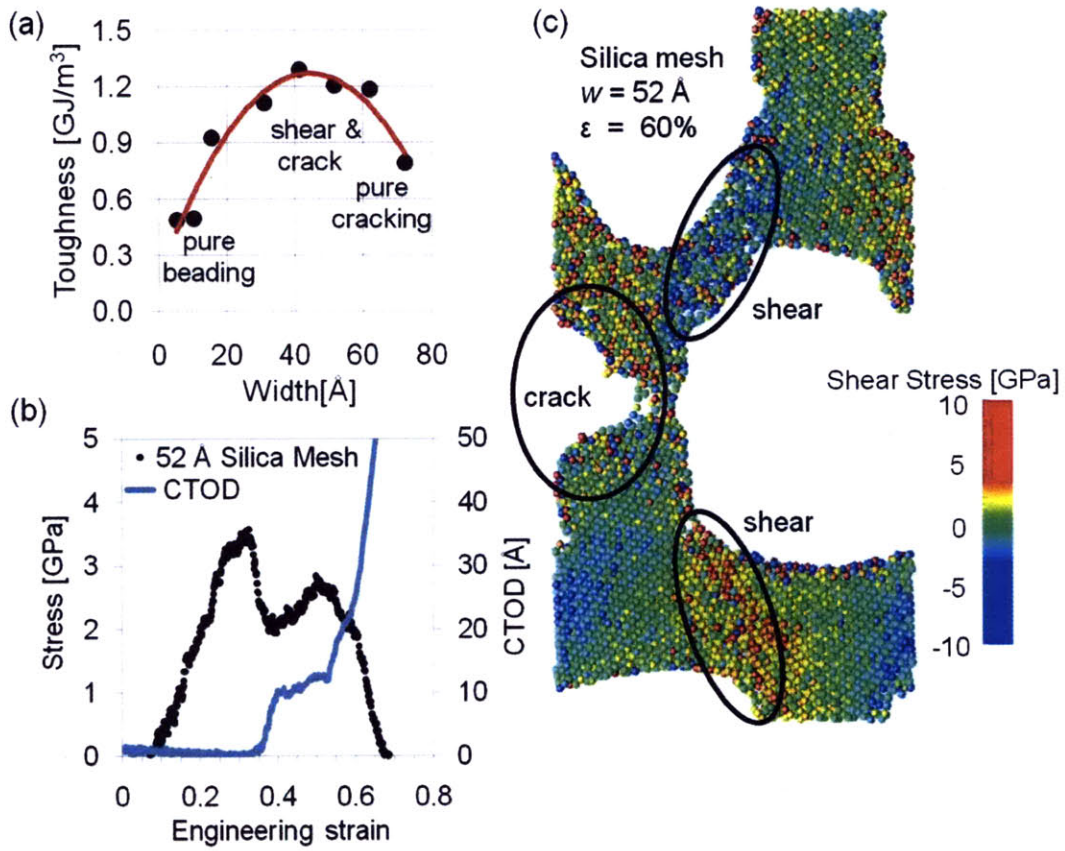

Figure 4-7: Panel (a): Toughness map with corresponding failure mechanism for the silica mesh. Panel (b): Toughening and stiffening mechanisms are caused by competing mechanisms of shear and crack formation. The crack tip opening displacement (CTOD) measurement reveals crack arrest and is plotted against the corresponding stress-strain data which reveal how well correlated both mechanisms are. Panel (c) shows the locations of shear and crack formation. For purposes of clarity, only the silicon atoms are shown.

modulus, reaching 36 GPa and 29 GPa for silicon and silica meshes, respectively. The effect of hierarchy on toughness is quite striking because the foil does not show a size-dependent toughness peaking response, as was observed for the meshes, and because it has a consistently lower toughness than the meshes. For example, the maximum toughness observed in silicon and silica meshes are 1.20×10^9 J/m^3 and 1.29×10^9 J/m^3, respectively, yet the silica foil reaches only 0.60×10^9 J/m^3. The reason for greater toughness in the higher hierarchy of meshes lies in competing mechanisms of shear and crack, wherein crack arrest is achieved either through shearing of another foil subcomponent in the mesh structure (as observed in the silica mesh, $w = 52$ Å), or through simultaneous cracking of different regions (as observed in the silicon mesh, $w = 43$ Å). These competing mechanisms are enabled through the hierarchical assembly of the foil elements into the mesh structure, and could not be achieved in unit foil structures alone. This result demonstrates that including higher levels of hierarchy are beneficial in improving the mechanical properties and deformability of silica structures.

4.3.1 Surface reconstruction

Surface reconstruction may occur and may have some effect on the mechanical behavior. For example, a previous molecular dynamics study reported a stiffening of silicon nanowires once the surfaces were reconstructed [92]. For a 1.05 nm thick nanowire, the modulus increased from approximately 150 GPa to 160 GPa once the [001] surface was reconstructed. The authors attributed this stiffening effect from bond saturation as reconstruction takes place. A previous study used ReaxFF and observed reconstruction of a ZnO surface after 300 ps at 700 K [74]. In another study, it was shown that a total time-scale of 240 ps was required to obtain a reconstructed silicon surface by an annealing process with the Tersoff potential and a total system size of 308 atoms [57]. Although it is expected that our ReaxFF based approach can capture surface reconstruction in principle, it is computationally expensive to capture this due to associated time-scale and system size, and was thus not observed in our simulations. Indeed, for small systems such as 1,000 atoms, ReaxFF could feasibly

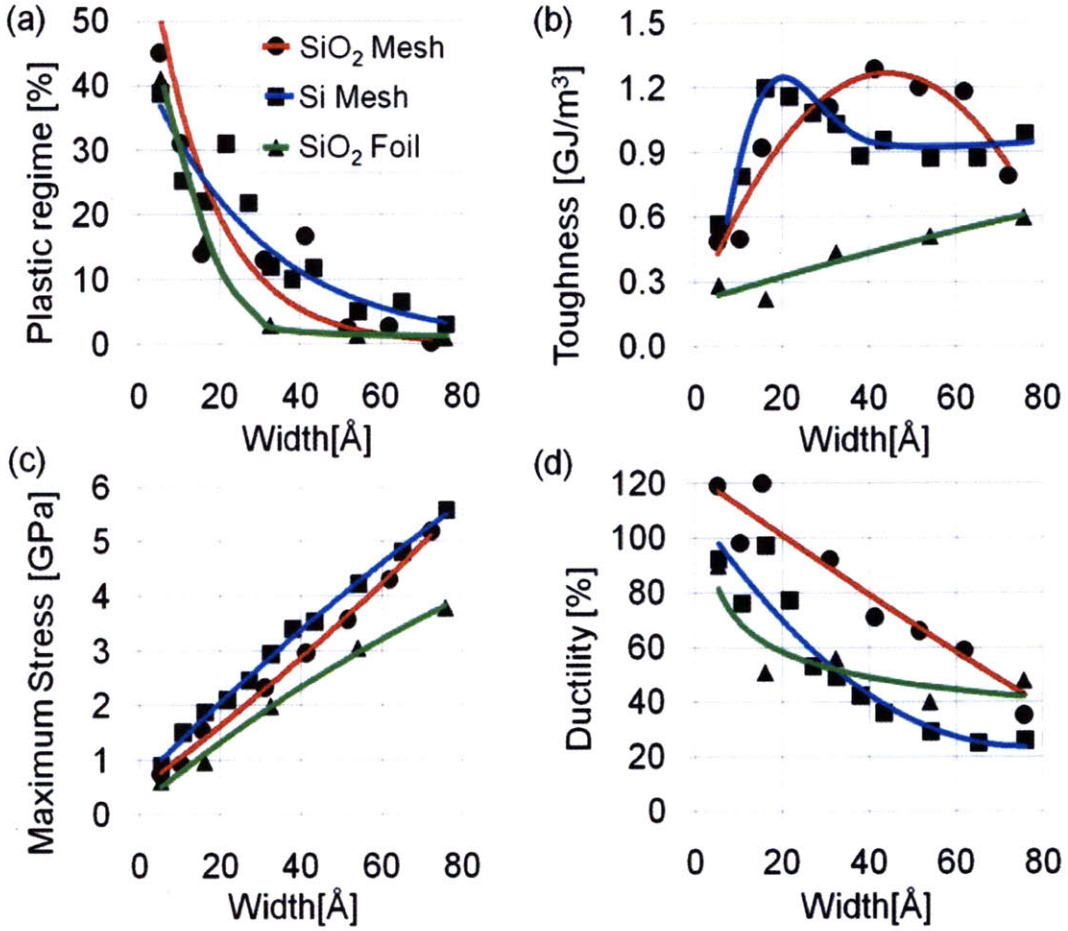

Figure 4-8: Comparison between silica mesh, silicon mesh, and silica foil structures showing the effect of wall width on (a) the plastic regime, (b) toughness, (c) maximum stress, and (d) ductility. Data for the nanoporous silicon is retrieved from [34]. Both the maximum stress and modulus are found to increase with the wall width. The ductility generally increases for smaller wall widths. The plastic regime is estimated by measuring the length of the linear plateau region which is associated with constant stress. In silicon, for wall widths larger than 27 Å, the toughness plateaus at around at 9×10^8 J/m^3. Between 16 Å and 27 Å a sharp increase in toughness is observed, with a maximum at $w \approx 16$ Å. Below 16 Å, the toughness drops to around 7×10^8 J/m^3, denoting an inverse trend. In the silica mesh the highest toughness is observed for wall widths of 41 Å, reaching values $\approx 1.29\times10^9$ J/m^3. The silica foil generally increases in toughness with the wall width, yet has lower toughness when compared to the mesh structures. Thus, by increasing the level of hierarchy, a higher toughness, maximum stress, and modulus can be achieved.

simulate the time scales listed above. However, for systems larger than 10,000 atoms, ReaxFF would be very computationally expensive. The investigation of surface reconstruction and its effects on the mechanics of hierarchical silica structures could be an interesting subject of future studies.

4.3.2 Preliminary investigation on the impact of the mechanical response from termination of silica

When exposed to a natural environment, silica surfaces generally become terminated with hydrogen after exposure to moisture. Results have been obtained in previous studies of silica nanorod deformation in the presence of water using semi-empirical quantum mechanics methods [79], where the authors concluded that strained siloxane (Si–O–Si) bonds are attacked by water which results in lower stress and lower failure strain of the silica nanorod, compared to a dry silica nanorod.

In the following investigation we consider two cases of silica surfaces: 1) bare silicon surfaces that are under coordinated, herein referred to as non terminated, and 2) hydrogen bonded to a surface of oxygen, herein referred to as non terminated. Two geometries are considered, foils of w=15 Å and meshes of w=5 Å. One common process by which surface termination is achieved is through contact with water to the silicon surface dangling bonds of silica. The water dissociates into OH and H, with the hydroxide bonding to the silicon. In our simulations, all structures are equilibrated under the canonical ensemble at 300 K for a time of 10 ps and then loaded under uniaxial strain loading along the [1 2 0] direction at a strain rate of 1×10^{10} s^{-1} at 300 K. The system has periodic boundary conditions in all three directions and the temperature is controlled by the Berendsen thermostat [7]. Deformation is applied by uniaxially increasing the size of the periodic simulation cell in the loading direction only, while keeping all other dimensions of the simulation cell constant. We use a time step of 0.2 femto-seconds. The initial, unstrained silica structure is shown in Figures 4-9 and 4-10.

As the terminated structures are stretched, the surfaces form various types of

polymorphs with geminal and interacting silanols as the most common. The non terminated foils have a greater maximum stress than that of the terminated foil, 1.38 GPa versus 1.21 GPa, respectively, as shown in Table 4.1 and Figure 4-9. Ductility is reduced from 67.2% to 66.2% as the foil is terminated. The results of lowering ductility and types of observed polymorphs are consistent with other studies [79, 64].

As the meshes are stretched, termination allows a ductility of 250% versus 122% for non terminated, as shown in Table 4.2 and Figure 4-10. Since the terminated meshes are fully coordinated, the struts are thinned down to atom chains with a one silicon atom thickness that are symmetrical, whereas the non termianted meshes form amorphous like struts that fail earlier. Also, the hydrogens atoms do not seem to break any Si–O–Si bonds, thus offering another explanation for the hight ductility.

	H Terminated	**Si Surface**
max stress [GPa]	1.21±0.01	1.38±0.037
strain at max stress [%]	35±0.5	48±5
failure strain [%]	66.2±3.6	67.5±5

Table 4.1: Comparison between H terminated and Si surface foils of ductility, maximum stress, and strain at maximum stress).

	H Terminated	**Si Surface**
max stress [GPa]	0.84±0.008	0.69±0.023
strain at max stress [%]	244±4.5	105±5
failure strain [%]	250±4.1	122±7

Table 4.2: Comparison between H terminated and Si surface meshes of ductility, maximum stress, and strain at maximum stress).

4.4 Conclusion

By utilizing an atomistic simulation approach based on the first principles reactive force field ReaxFF, we have investigated the impact of hierarchical structures on the mechanical response of the most abundant mineral on earth, silica. By incorporating a hierarchical design concept inspired by diatoms algae, we have modeled two levels

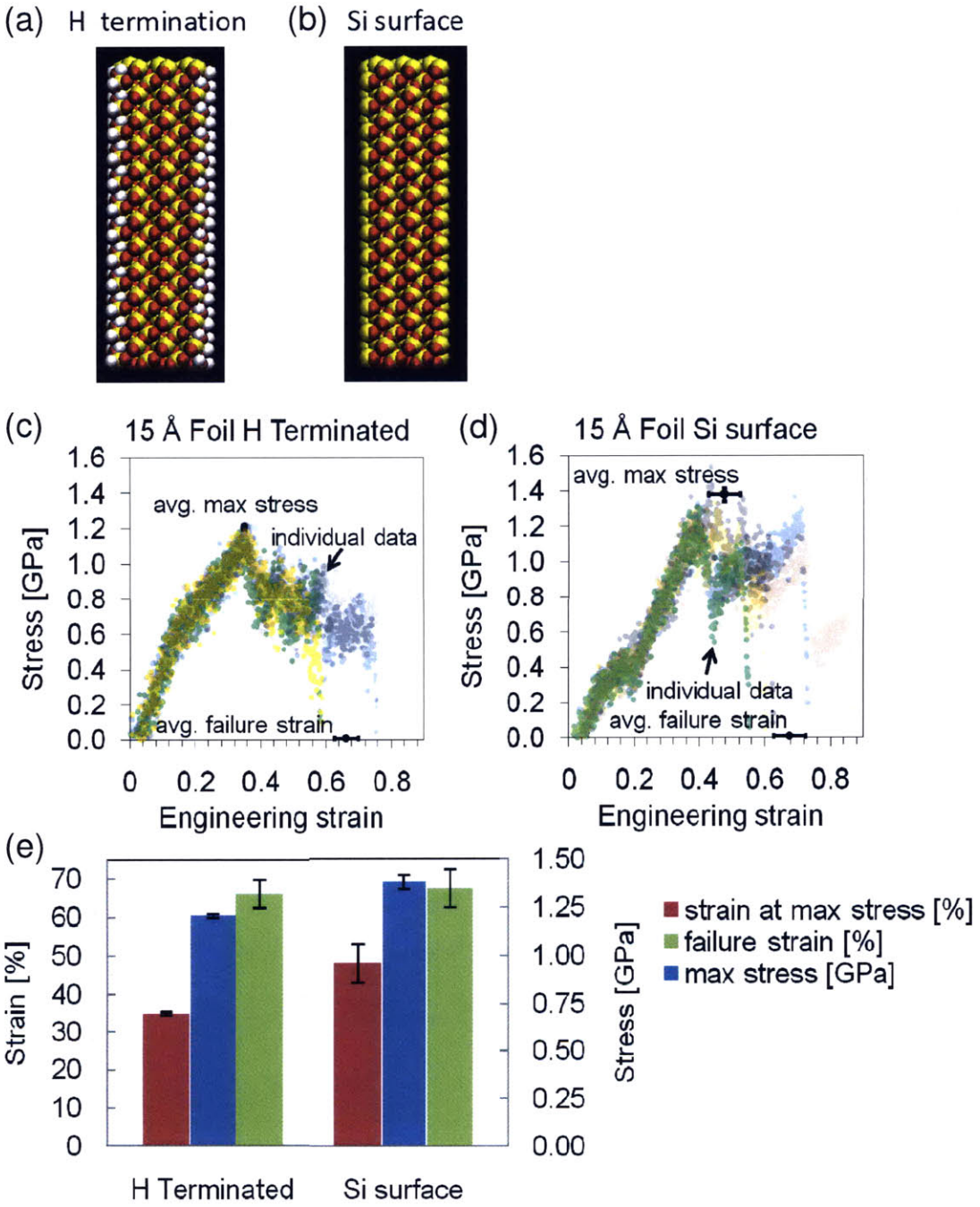

Figure 4-9: Comparison of terminated (a) and non terminated (b) 15 Å silica foils. The stress strain graph is shown for the terminated (c) and non terminated (d). The comparison of ductility, maximum stress, and strain at maximum stress is shown in (e). Once terminated the maximum stress decreases by approximately 0.17 GPa and low standard error of 0.5% compared to 5% of the non termianted case. The standard error of the mean, SEM, is determined from a total of five simulations for each of the terminated and non terminated cases. Termination decreases ductility by roughly 1.3%. Each color in the stress strain graph represent the individual runs.

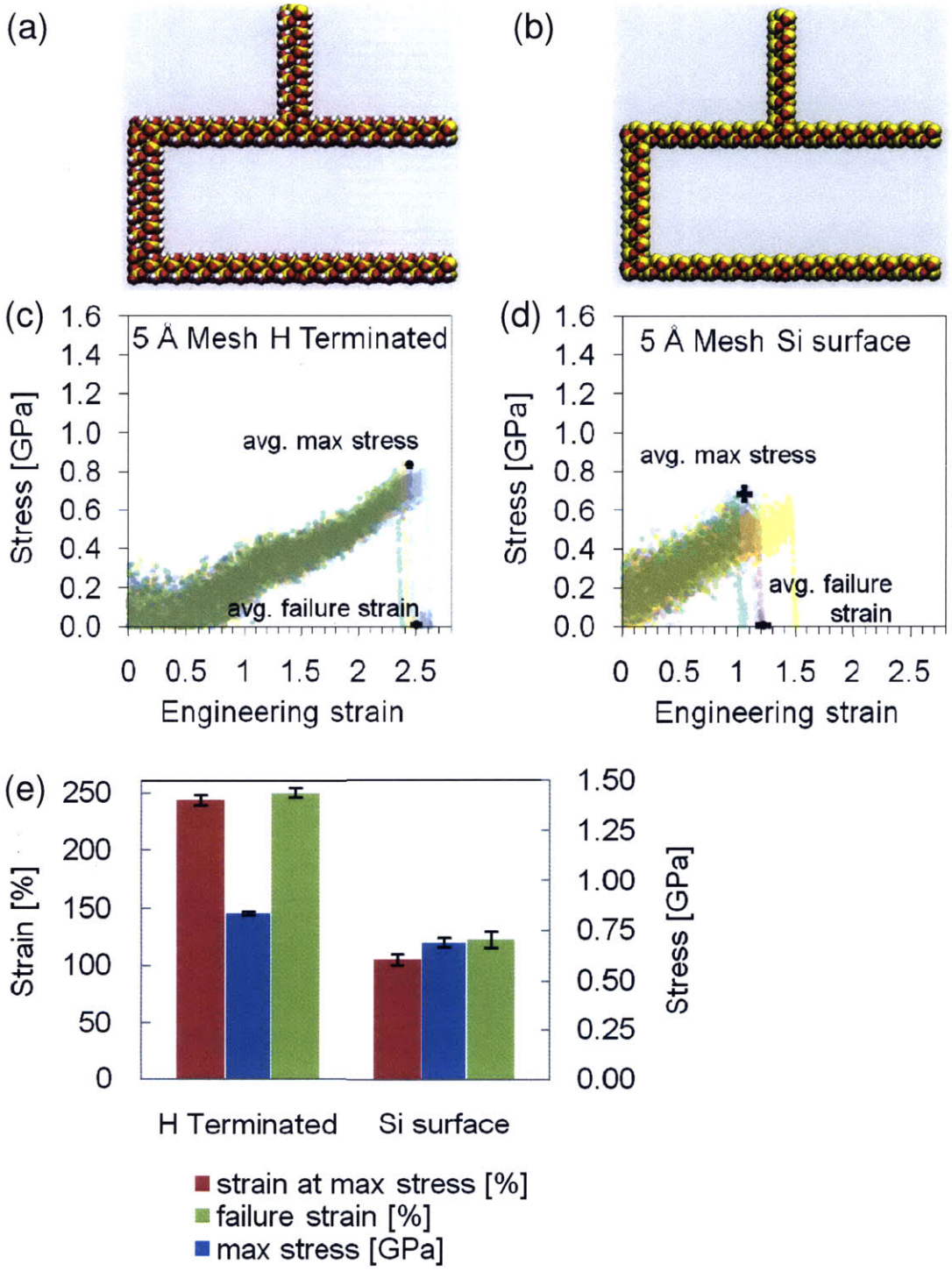

Figure 4-10: Comparison of terminated (a) and non terminated (b) 5 Å silica meshes. The stress strain graph is shown for the terminated (c) and non terminated (d). Once terminated, the maximum stress increases by approximately 0.15 GPa. The standard error of the mean, SEM, is determined from a total of five simulations for each of the terminated and non terminated cases. Termination drastically increases ductility from 122% to 250%, as shown in (e). Each color in the stress strain graph represent the individual runs.

of geometric hierarchies: (1) A nanoscale foil of silica, and (2) a nanoscale silica mesh composed of interlocking foils. These arrangements were then studied with different wall widths in order to reveal the effect of size-scaling on their mechanical properties. Next, we presented a comparison between the mechanical properties of silica meshes and silica foils. Our findings suggest that higher levels of hierarchy are critical to greatly improving toughness, and can increase toughness by up to 200% from silica foil to silica mesh.

We ascribe these magnificent improvements in mechanical properties of the mesh structures from two competing atomistic mechanisms of deformation; shear and brittle crack propagation. In the toughest silica mesh, for example, a crack arrests due to shearing of another strut, which consequently stiffens the system (see Figure 4-7). Interestingly, a size-dependent peaking of toughness was observed for the Si and SiO_2 meshes; with a maximum toughness of 1.29×10^9 J/m^3 corresponding to w = 41 Å for the SiO_2 mesh (see, Figure 4-8(b)). The increased toughness of these nanostructures also makes them viable candidates for impact-resistant lightweight structures, and this should be tested in further detail. Another powerful concept derived from this study is the ability to transform a brittle material into a ductile one by simply manipulating the geometry of a constituent structure to resemble that of ordered nanopores, or mesh. Three reasons for the high ductility are three-fold, (1) a homogeneous distribution of surface stress throughout the entire structure, (2) a conformational change from rectangular to hexagonal pores, and (3) competing mechanisms of shear and crack arrest.

In a similar fashion to structural materials found in nature, such as bone, nacre, or diatom shells, it seems that hierarchy is a cornerstone of nanomaterial design for superior mechanical properties. More importantly, the concept of hierarchical structures made of the same materials (as demonstrated in this article) is fundamental in order to fully realize the enormous potential of nanomaterial design. To the best of the authors' knowledge, this paper is the first to elucidate, at the atomistic scale and with near quantum mechanical accuracy, the complex mechanical response and failure mechanisms due to implementing hierarchy in silica. The key contribution

of this work is that by introducing structural hierarchies, a weakness can be turned to strength, that is, an intrinsically strong but brittle material becomes exceedingly tough, strong, and ductile. The fact that a similar behavior was found in silicon [34] suggests that this may indeed be a generic design concept that could be used for many materials The observation that a weakness is turned into strength is also reminiscent from recent findings of similar behaviors of H-bonds, which are by itself also highly brittle, weak elements but reach extreme levels of toughness and strength once arranged in particular hierarchical patterns [47].

Future research lies in addressing the impact of a larger number of hierarchy levels on the mechanical properties of silica nanostructures, and the effect of water on hierarchical silica.

Chapter 5

Superductile, wavy silica nanostructures

The previous chapters focused on the mesh structures found in many diatoms, such as *Bacillariophyceae*, and revealed the impact of hierarchy and size on the mechanical response. The next step in unraveling the interplay between structure and mechanical response of diatoms lies in understanding their fantastic ability to stretch while still being intact. The extreme ductility of certain diatom species and communities is a fascinating attribute, especially since diatoms are mostly made of amorphous silica, a typically brittle constituent. In this chapter we focus on a particularly interesting colonial diatom, *Ellerbeckia arenaria* because they live in waterfalls and are thus able to resist significant and continual mechanical stress. These colonies are also able to elastically stretch up to about 33% [36, 35]! Two possible reasons for this extreme mechanical response are the intrinsically shaped cell wall and the organic coating, called mucilage, surrounding the cell wall surface. In this chapter, a new geometry is analyzed due to its presence in certain diatoms species that are able to elongate and resist extreme mechanical stress from to the environment. We, therefore, focus on the corrugated, wavy shape found along the sides of *Ellerbeckia arenaria* (see Figure 5-1(a)), and propose that this particular shape is essential to providing flexibility while combining high strength and toughness [32].

5.1 Model geometry

We consider a structural design composed of alpha-quartz crystals. The structure is a foil or infinitely tall thin wall with varying amplitude and width, resembling a wave, as seen in Figure 5-1(b). Since the simulation box is periodic, the foil structure can be thought of an array of waves with a spacing equivalent to the peak-to-peak amplitude. The z axis has no free surface, and the structure can be described as infinitely tall. Figure 5-1(c) shows the geometries considered here. All wave structures have an equivalent wavelength of 63.5 Å. The only parameter varied here is the wall width w and amplitude A, which range from 20 Å to 120 Å, and 0 Å to 60 Å respectively (see Figure 5-1(c)). The number of atoms varies from $\approx$ 650 to $\approx$ 7000 for the smallest to the largest width silica systems. For the wave structures, the largest simulation cell has dimensions of 177 Å × 63.5 Å × 8.5 Å in the x-, y-, and z-direction.

5.2 Simulation approach

All structures are equilibrated under the canonical ensemble at 300 K for a time of 10 ps and then loaded under uniaxial strain loading along the [1 2 0] direction as shown in Figure 1(b), at a strain rate of 1×10^{10} s^{-1} at 300 K. The system has periodic boundary conditions in all three directions and the temperature is controlled by the Berendsen thermostat [7]. Deformation is applied by uniaxially increasing the size of the periodic simulation cell in the loading direction only, while keeping all other dimensions of the simulation cell constant. We use a time step of 0.2 femto-seconds. The initial, unstrained silica structure is shown in Figure 5-1(c). Aside from the variations in the geometry, all simulations are carried out under identical conditions, enabling us to perform a systematic comparison.

5.3 Results and discussion

Here we present our analysis on the effect of altering the amplitude and wall width on the mechanical properties of the silica wave structures (see Figure 5-1(c) for the two

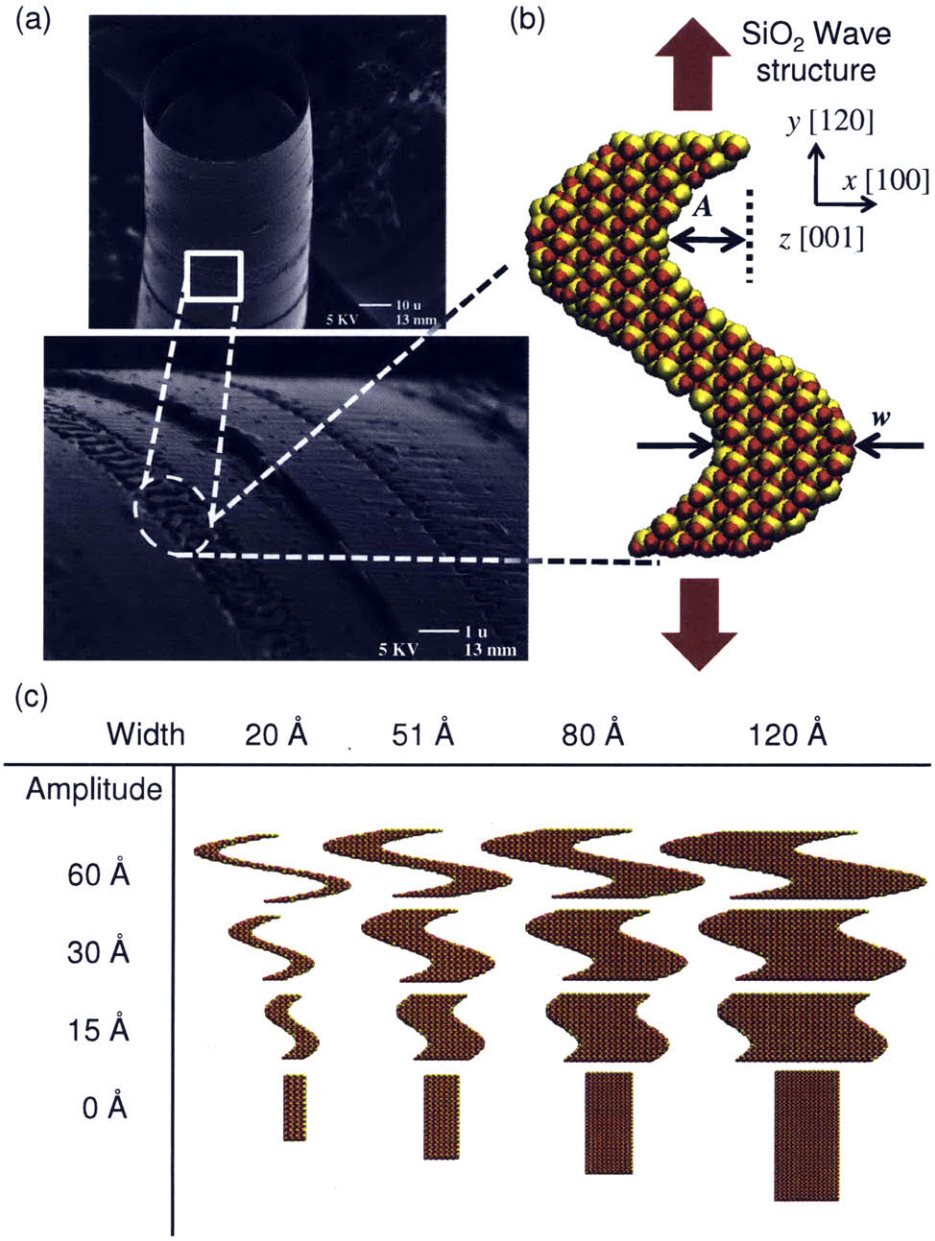

Figure 5-1: Panel (a): A colonial diatom, *Ellerbeckia arenaria*, lives in waterfalls and contains girdle bands with intricate patterns. Specifically, a wave shape can be seen, which might be an important contribution to the elastic response of approximately 33%, as observed through AFM experiments [36]. Panel (b): Initial geometry of a bioinspired silica structure used in our simulations, illustrating the wall width and amplitude (w and A, definitions indicated in the structure). Panel (c): Initial geometry of all wave structures considered here, illustrating the range of variation in amplitude and width. Images reprinted from Ref. [36], Gebeshuber, et al. Journal of Nanoscience and Nanotechnology 2005 [permission pending].

geometries considered). As shown in Figure 5-1(c), the wall width w and amplitude A, which range from 20 Å to 120 Å, and 0 Å to 60 Å respectively. These structures resemble those found in some diatoms, such as *Ellerbeckia arenaria.*

The stress strain response for all structures is shown in Figure 5-2. Here we observe a maximum strain of 270% for the structures with largest amplitude, 60 Å and w of 51 Å and 80 Å. Interestingly, the initial modulus of these structures is roughly ten times lower than those with lower amplitude. For structures with largest width and lowest amplitude, the greatest modulus and maximum stress are reached: $E = 14.4$ GPa and $\sigma_{\max}$= 5 GPa. The general trend is for decreasing failure strain, and greater modulus and maximum stress as the wall width is increased and the amplitude is lowered.

Next, we analyze the effect of altering the wall width and amplitude on the toughness, ductility, maximum stress, and modulus, as seen in Figure 5-3. The toughest response is seen for amplitudes below 30 Å and greater than 51 Å. It is important to note that these structures are defect free, and thus the upper limit on toughness can diverge from experimental ones. Ductility is highest, reaching ≈270%, for amplitudes of 60 Å, and 51 Å $\leq w \leq$ 80 Å. The largest maximum stress is found for 0 Å $\leq A \leq$ 15 Å of and 80 Å $\leq w \leq$ 120 Å. Toughness versus modulus is compared in Figure 5-3 (c), showing that they are both positively correlated for decreasing amplitude. However, the increased toughness and modulus comes at the expense of ductility. The structure with greatest toughness of 1.3 GJ/m^3 corresponds with a relatively low ductility of ≈50%.

The observed deformation mechanisms are closely linked to the mechanical response of each structure. In Figure 5-4 we compare the Von Mises stress fields of three structures and the corresponding deformation mechanisms during failure which correlate with three distinct mechanical responses: high toughness, high ductility, and high stress. The structure with highest toughness is shown in Figure 5-4 (a), and contains a significant portion of the stress to form a straight line, and lower stress near the curved regions. As failure occurs, cracking initiates near the corners and propagates in a diagonal shearing fashion. Void formation dictates the path of cracking,

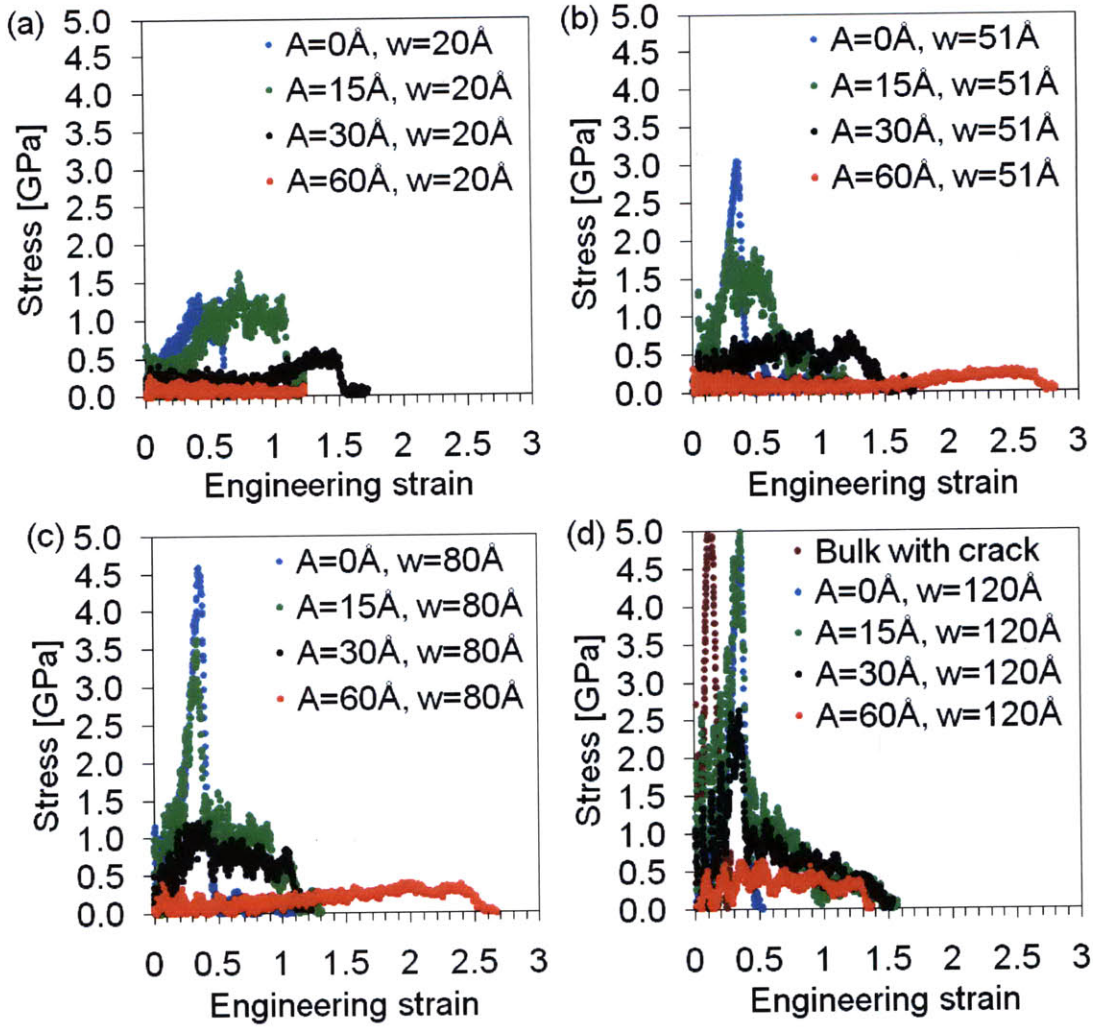

Figure 5-2: Stress-strain graph of silica wave structures, for $w = 20$ Å panel (a), $w = 51$ Å panel (b), $w = 80$ Å panel (c), and $w = 120$ Å panel (d). Panel (a): The structures of lowest width, 20 Å, resist a maximum stress of 1.5 GPa, seen in $A = 20$ Å. For $A = 60$ Å, $w = 20$ Å, the structure fails immediately upon loading. In $A = 30$ Å, $w = 20$ Å, the structure unfolds and straightens, thus allowing for steep increase and plateau in stress at 100% strain. Panel (b): The structures with amplitudes of 15 Å and 30 Å increase in brittleness when the wall width is increased. However, for $A = 30$ Å the ductility is drastically increased to 283% strain. The gradual increase in stress indicates subtle unfolding and eventual straightening of the structure. Panel (c): As wall widths are increased to 80 Å the maximum stress rises for all structures, but also fails sooner than structures with smaller widths. Panel (d): The highest stress is observed, reaching 5 GPa for $A = 15$ Å, $w = 120$ Å. However, brittleness increases dramatically and the unfolding mechanisms is no longer observed for $A = 60$ Å, $w = 120$ Å, which fails at 130% strain. Failure mechanisms characteristic of the most brittle structures, such as $A = 15$ Å, $w = 120$ Å, are crack and shear, along with void formations that coalesce with other voids until the structure is no longer intact. Bulk silica has many defects which allow for its brittle nature. We performed a simulation of periodic bulk silica with a penny shaped crack 5 Å wide and 120 Å long, that extended through 120 Å of silica, that failed at 12% strain and reached a maximum stress of 5.3 GPa.

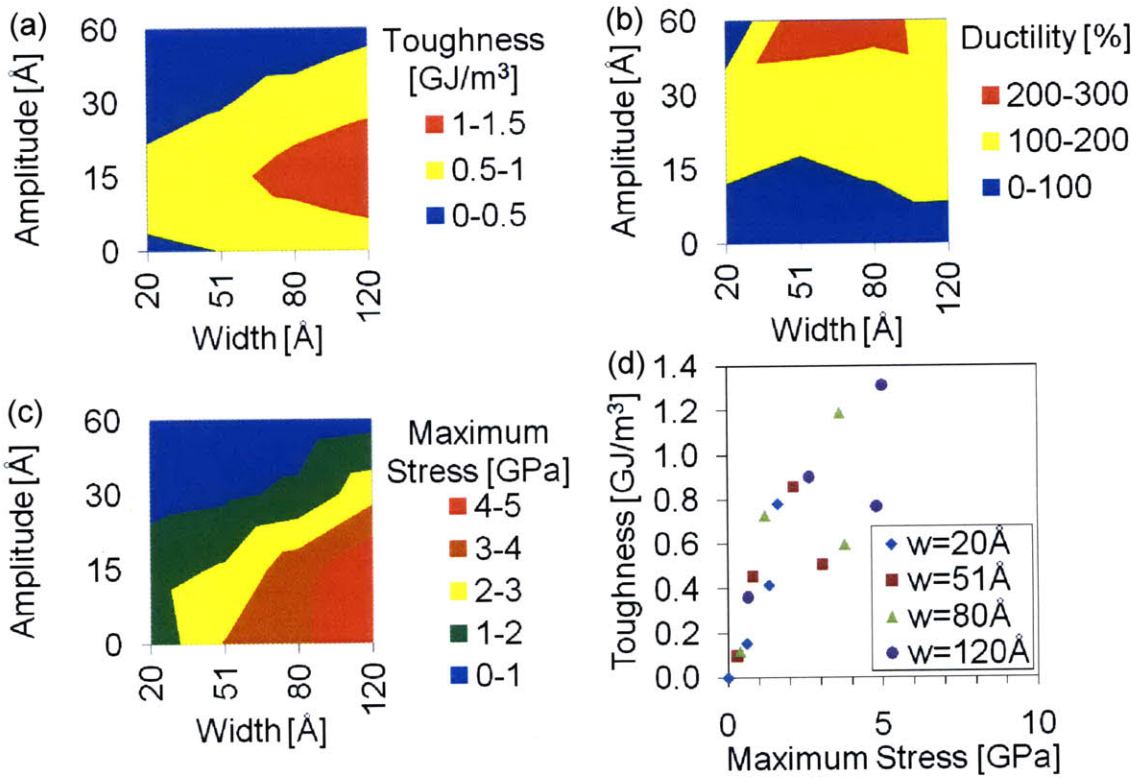

Figure 5-3: Panel (a): Toughness map, showing that greatest toughness is achieved for structure with $A = 15$ Å, $w = 120$ Å. Panel (b): Ductility map. Structures with greatest ductility have the highest amplitude, reaching up to 283%. However, as the amplitude becomes 0-15 Å, ductility is generally below 100%. Panel (c): Maximum stress map, showing that structures with lowest amplitude and large width, such as $A = 15$ Å, $w = 120$ Å, reach a stress up to 5 GPa. Panel (d): Nonlinear relationship between modulus and maximum stress. The structure with greatest toughness is $A = 15$ Å, $w = 120$ Å.

while the shearing effect breaks off the outermost surface of the voids in a sequential manner, similar to a beading mechanism. For structures with highest ductility, the deformation path is unfolding and finally beading. The unfolding mechanism encompasses the straightening of the central, or core structure, while the wave peaks remain in the initial conformation and open up slightly. Rotation of the core region is enhanced by single void formation near the corners. The core region is defined as the area bounded by the inner peaks of the wave. For structures with maximum stress, the deformation mechanism is mainly cracking, with very little shear deformation.

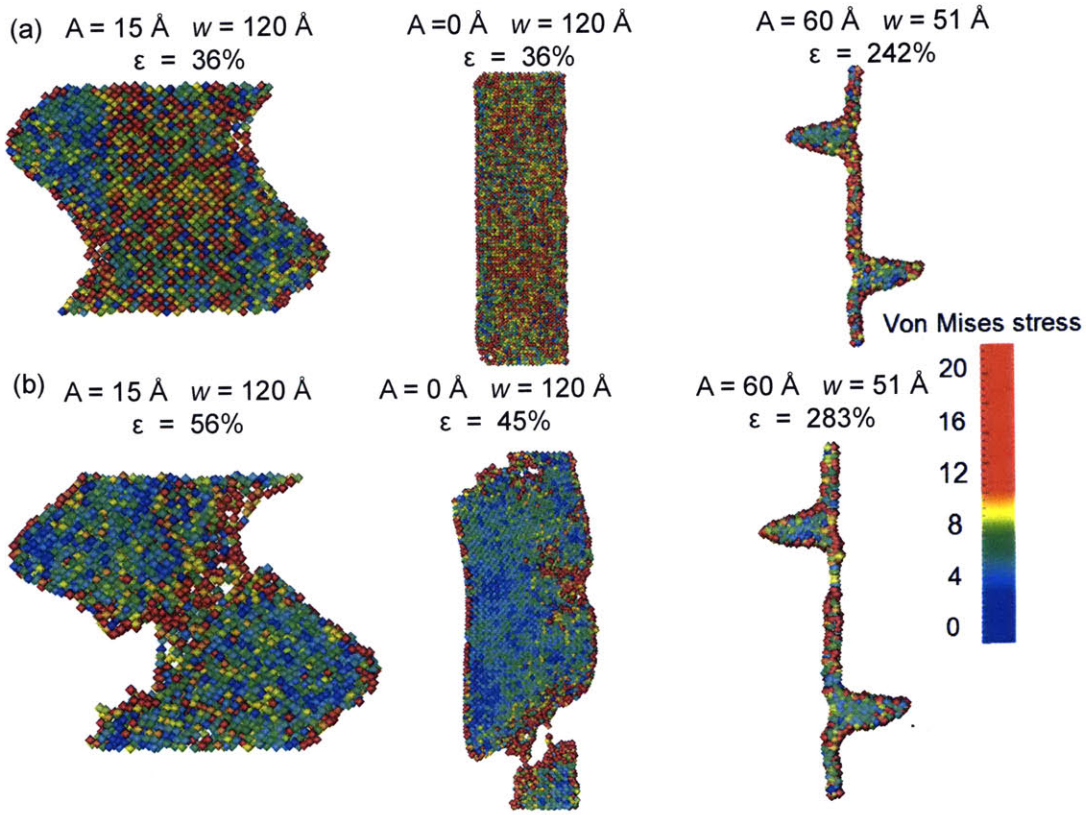

Figure 5-4: Von Mises stress field for structures at maximum stress, panel (a), and at failure, panel (b). Panel (a): The structure with $A = 15$ Å, $w = 120$ Å contains a significant portion of the stress to form a straight line, and lower stress near the curved regions. For $A = 0$ Å, $w = 120$ Å the stress is relatively homogeneous, with highest stress on the surface. For $A = 60$ Å, $w = 51$ Å high stress is concentrated along the extended, vertical ligaments. Panel (b): High stress is observed near the failure process zone for the structure with $A = 15$ Å, $w = 120$ Å. The structure forms voids near the corner and shearing occurs next. For $A = 0$ Å, $w = 120$ Å, failure is mainly crack formation, while unfolding and beading is observed for $A = 0$ Å, $w = 120$ Å.

Next, we map the regions of best performance – ductility, toughness, and maximum stress – and its relationship with the amplitude and width, as seen in Figure 5-5. For structures with high amplitude and low width, greatest ductility is achieved; whereas low amplitude and high width is yields the greatest strength. The structures of highest toughness have a width and amplitude bounded by the regions of highest ductility and stress. Interestingly, it is a balance of both geometric parameters (A and w) and a combination of deformation mechanisms (unfolding, shearing, and cracking) which allow for greatest toughness. Furthermore, this concept of geometric effects on the stress-strain behavior are displayed in Figure 5-6.

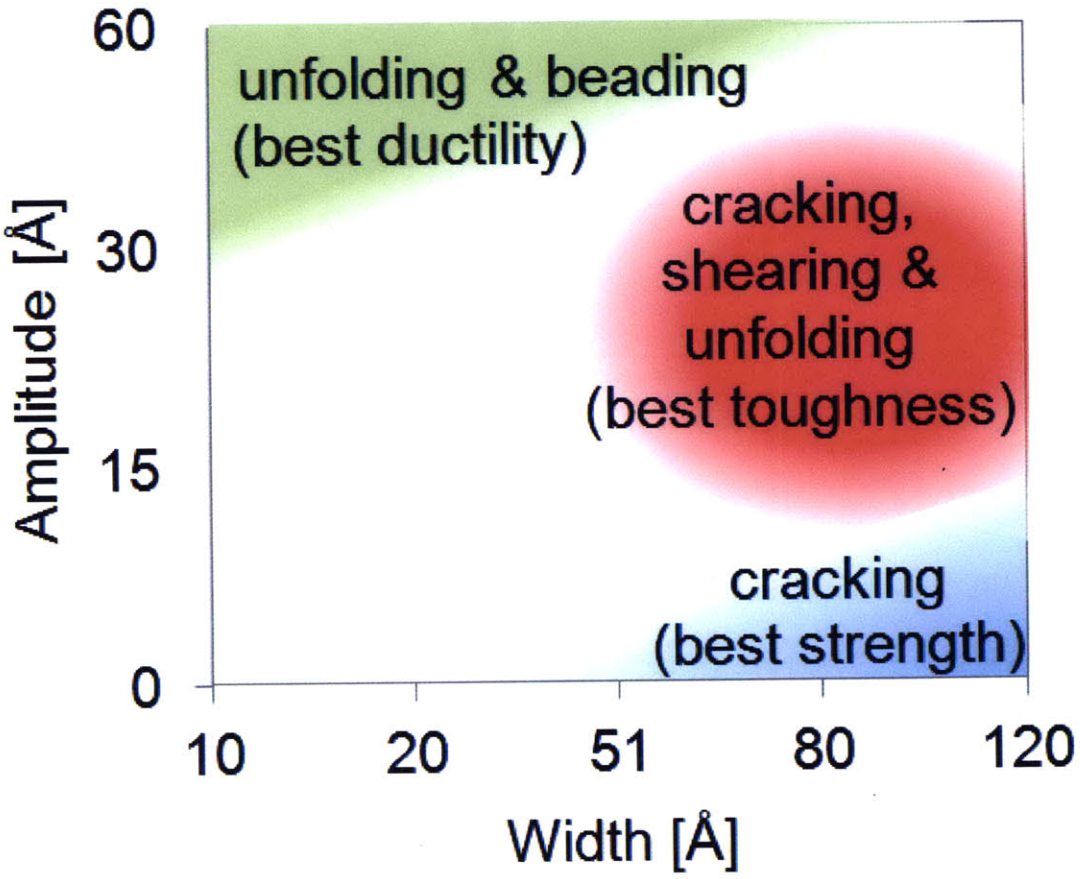

Figure 5-5: Performance map, showing the regions where optimum toughness, ductility, and strength are located with respect to width and amplitude.

An analogy to protein structures can be drawn, wherein sacrificial bonds and

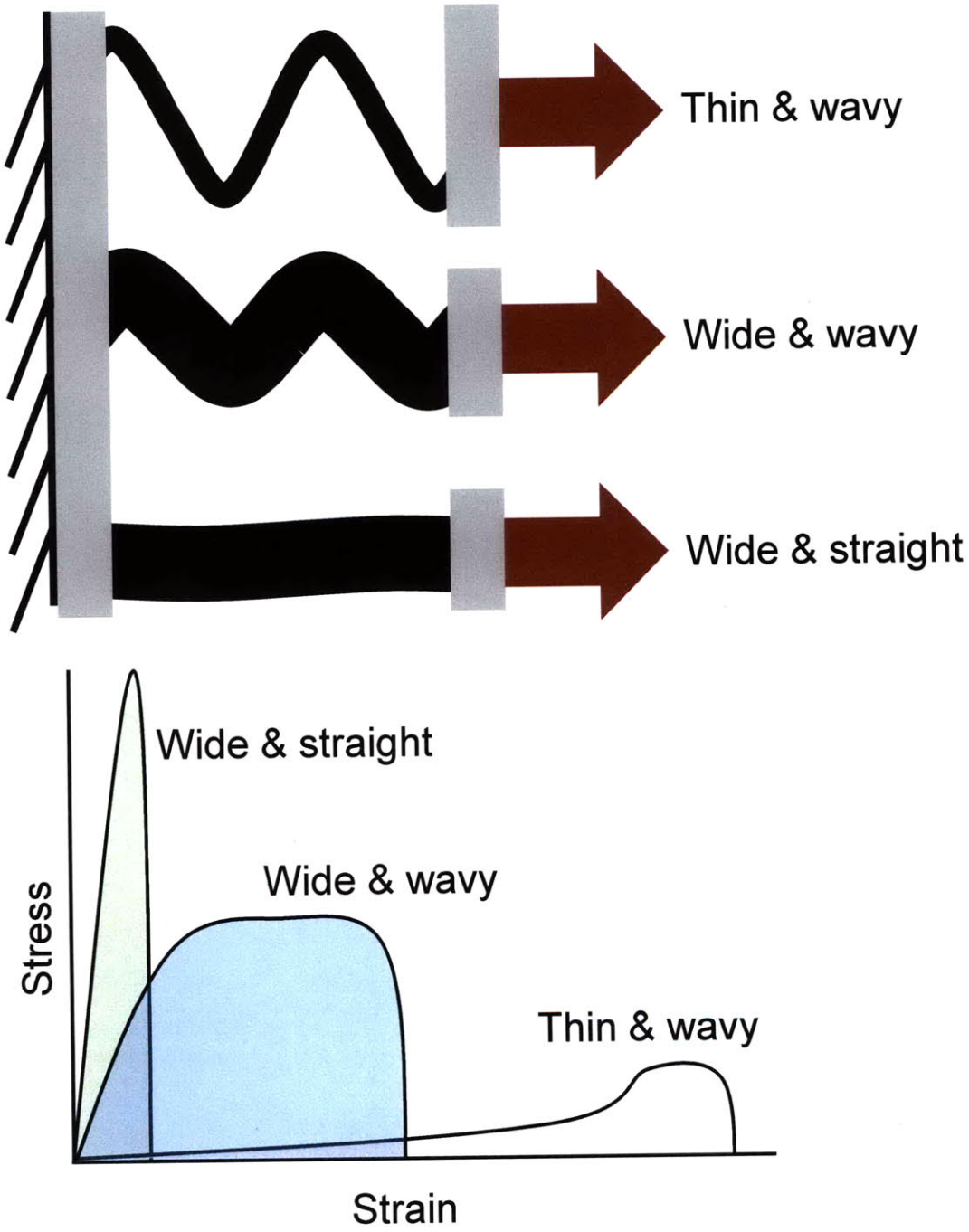

Figure 5-6: Schematic of stress strain response for tensile deformation of different morphologies of silica waves. Thin and wavy structures provide greatest ductility, while wide and straight structure provide high stress at the cost of ductility. However, when combining wavy and wide morphologies, significant toughness is gained.

hidden lengths are responsible for enhanced toughness [27, 81, 16]. These sacrificial bonds are weaker than the carbon backbone, but stronger than van der Waals or hydrogen bonds, and allow for saw-tooth shape force-extension curves. Sulfate bonds are a great example of sacrificial bonds in systems containing DOPA, a common amino acid found in biological adhesives. As each sacrificial bond breaks, energy is released in the form of heat and a regional unfolding, or uncoiling of a hidden length segment, occurs. This process is repeated until all the sacrificial bonds are broken and the structure is completely unfolded. Only then will the carbon backbone break, resulting in the highest peak of stress. The interplay of multiple failure zones and deformation mechanisms is strikingly similar to those found in the silica wave structures. A link is made between the sacrificial bonds found in proteins, and the shearing mechanism found in the silica wave. The catastrophic carbon backbone failure is also analogous to cracking in a silica system. When integrating these multiple mechanisms, a universal concept of enhancing toughness is achieved.

5.4 Conclusion

In summary, we have investigated the fundamental impact of wave structure geometries on the mechanical response of silica, by utilizing an atomistic simulation approach based on the first principles reactive force field ReaxFF. Specifically, we are able to demonstrate that the ductility of silica can reach to approximately 270%, by increasing the amplitude to 60 Å and maintaining the width at 51 Å. This is achieved by unfolding mechanisms and straightening of the structure, similar to the uncoiling of hidden length from a convoluted protein. The structures with greatest toughness, reaching values of up to 1.3 GJ/m^3, have a 15 Å amplitude and a 120 Å width. And finally, greatest strength is obtained from straight and widest, $w = 120$ Å, structures.

Indeed, the study in this chapter is an important step towards revealing the broad range of mechanical properties achieved through altering specific geometric shapes (s.a. mesh to wavy), and will undoubtedly pave a conceptual figure of merit for future nanoscale structural designs. Discovering that silica can indeed become extremely

ductile opens opportunities for industrial applications, such as flexible nanoscale processors, and offers new incentives, in terms of mechanical response, for the incorporation and fabrication of wavy silica structures.

Chapter 6

Conclusion

The ability to improve upon multiple mechanical properties, such as toughness, strength, and ductility, is extremely important when designing future nanoscale materials. Altering the mechanical properties of one of the most brittle and abundant minerals on earth, silica and silicon, allows a new window of opportunity for humanity to create applications and reinvent materials once thought to be impossible. The transferability of the concept allowing for massive transformation of mechanical responses, such as brittle to ductile or weak to tough, through geometric alterations at the nanoscale, is another profound discovery that will undoubtedly unleash a new paradigm in the way materials are designed and applied. Indeed, the culmination of materials design is to maintain environmental sustainability, infrastructure superiority, multifunctional capacity, and economic feasibility. Nanoscale materials implemented through design and fabrication concepts found in biology, such as in diatom algae, bone, and sea sponges, hold the promise of providing these advantages.

6.1 Summary of findings

Revealing the intricate interplay between structure and mechanical response of diatoms requires delicate and systematic analysis. The previous chapters established a framework on size effects, hierarchy, and shape, on the mechanical response of silicon and silica structures. The main findings are summarized as follows:

- Silicon and silica meshes yield highly tunable mechanical properties through alteration of their width, as shown in Figure 4-8 . A region of optimum toughness is observed to lie between w=20 Å and w=50 Å. Crack arrest and shear mechanisms allow for the high toughness, as shown in Figure 4-7.

- Hierarchical structures, such as meshes, have superior toughness and ductility when compared to their constituent counterparts, foils, as shown in Figure 4-2. The foils lack the multiple mechanisms of failure that are observed in the meshes.

- Wavy silica structures are able to reach extremely high ductilities of up to $\approx$ 270%, as shown in Figures 5-3 and 5-4, through unfolding mechanisms and straightening of the structure, similar to the uncoiling of hidden length from a convoluted protein.

6.2 Discussion and future research

Several challenges remain in the form of fabricating and more accurately modeling these structures. For example, biomineralization from self assembling proteins which guide silica precipitation has been studied [53, 52, 86, 85]. However, the ability to synthesize complex and hierarchical structures still remains challenging. The recent determination of certain diatom genetic sequences will further the understanding of accurately controlling and fabricating silica structures. In terms of modeling these systems, a key consideration is the effect of surface reconstruction on the mechanical properties. However, surface reconstruction occurs on timescales that are intractable for many atomistic methodologies, such as ReaxFF or quantum based approaches.

Future research could be geared toward atomistic simulations on the deformation and failure of different morphologies found in diatom species. Moreover, mineralized structures are found in many other biological systems, such as deep see sponges [2], which could be studied using a similar molecular approach.

Another important step is reaching a greater convergence between actual diatom

frustules and those modeled. Key challenges are reaching greater size scales, incorporating organic material, amorphization, and surface termination. The size scale issue can be generally overcome with coarse graining, or utilizing massive supercomputers on the order of hundreds of cpu's with ReaxFF. With larger systems, more complex shapes can be modeled, such as incorporating different shapes throughout the z axis. Perhaps a more complicated challenge is the addition of organic material, such as proteins, within the silica structure. The existing ReaxFF forcefield that models both organics and silica is limited to glyoxal, and does not encompass nitrogen bonds, an element found in many organic structures, such as collagen [51]. Once the adequate forcefield is developed, proteins such as silaffins and collagen could be added to the silica. As previous studies have mentioned, proteins within diatoms are found in their adhesives and enable self assembling [22]. Amorphization of silica is another critical concept that should be explored, since it could affect the mechanical properties and is also found in diatoms. Another avenue for further research is surface termination, as it occurs when silica is exposed to water, and does affect the mechanical response of silica structures, as observed in the preliminary investigation in this thesis. Future simulations of surface terminated structures will encompass larger systems in order to more fully capture the effect at different length scales.

Bibliography

[1] J. Aizenberg. Crystallization in patterns: A bio-inspired approach. *Advanced Materials*, 16(15):1295–1302, 2004.

[2] J. Aizenberg, J. C. Weaver, M. S. Thanawala, V. C. Sundar, D. E. Morse, and P. Fratzl. Skeleton of euplectella sp.: Structural hierarchy from the nanoscale to the macroscale. *Science*, 309(5732):275–278, 2005.

[3] B. Alder and T. Wainwright. Phase transition for a hard sphere system. *The Journal of Chemical Physics*, 27(5):1208–1209, 1957.

[4] J. T. Allen, L. Brown, R. Sanders, C. Mark Moore, A. Mustard, S. Fielding, M. Lucas, M. Rixen, G. Savidge, S. Henson, and D. Mayor. Diatom carbon export enhanced by silicate upwelling in the northeast atlantic. *Nature*, 437(7059):728–732, 2005.

[5] E. V. Armbrust, J. A. Berges, C. Bowler, B. R. Green, D. Martinez, N. H. Putnam, S. Zhou, A. E. Allen, K. E. Apt, M. Bechner, M. A. Brzezinski, B. K. Chaal, A. Chiovitti, A. K. Davis, M. S. Demarest, J. C. Detter, T. Glavina, D. Goodstein, M. Z. Hadi, U. Hellsten, M. Hildebrand, B. D. Jenkins, J. Jurka, V. V. Kapitonov, N. Kroger, W. W. Y. Lau, T. W. Lane, F. W. Larimer, J. C. Lippmeier, S. Lucas, M. Medina, A. Montsant, M. Obornik, M. S. Parker, B. Palenik, G. J. Pazour, P. M. Richardson, T. A. Rynearson, M. A. Saito, D. C. Schwartz, K. Thamatrakoln, K. Valentin, A. Vardi, F. P. Wilkerson, and D. S. Rokhsar. The genome of the diatom thalassiosira pseudonana: Ecology, evolution, and metabolism. *Science*, 306(5693):79–86, 2004.

[6] M. F. Ashby. Materials selection in mechanical design, third edition. *http://owens.mit.edu/sfx_local?bookid = 25372rft.genre = booksid = Barton : Books24x7*, 2005.

[7] H. J. C. Berendsen, J. P. M. Postma, W. F. van Gunsteren, A. DiNola, and J. R. Haak. Molecular dynamics with coupling to an external bath. *The Journal of Chemical Physics*, 81(8):3684–3690, 1984.

[8] D. Bonamy, S. Prades, C. Rountree, L. Ponson, D. Dalmas, E. Bouchaud, K. Ravi-Chandar, and C. Guillot. Nanoscale damage during fracture in silica glass. *International Journal of Fracture*, 140(1):3–14, 2006.

[9] M. Buehler, J. Dodson, P. Meulbroek, A. Duin, and W. Goddard. The computational materials design facility (CMDF): A powerful framework for multi-paradigm multi-scale simulations. *Mat. Res. Soc. Proceedings*, 894:LL3.8, 2006.

[10] M. Buehler, A. Duin, and W. Goddard. Multi-paradigm modeling of dynamical crack propagation in silicon using the reaxff reactive force field,. *Phys. Rev. Lett.*, 96(9), 2006.

[11] M. Buehler and S. Keten. Colloquium: Failure of molecules, bones, and the earth itself. *Reviews of Modern Physics*, 82(2):1459, 2010.

[12] M. J. Buehler. Large-scale hierarchical molecular modeling of nano-structured biological materials. *J. Comput. Theor. Nanosci.*, 3(5):603–623, 2006.

[13] M. J. Buehler. *Atomistic modeling of materials failure.* Springer, New York; London, 2008.

[14] M. J. Buehler and T. Ackbarow. Fracture mechanics of protein materials. *Materials Today*, 10(9):46–58, 2007.

[15] M. J. Buehler, H. Tang, A. C. T. van Duin, and W. A. Goddard. Threshold crack speed controls dynamical fracture of silicon single crystals. *Physical Review Letters*, 99(16):165502, 2007.

[16] M. J. Buehler and Y. C. Yung. Deformation and failure of protein materials in physiologically extreme conditions and disease. *Nat Mater*, 8(3):175–188, 2009.

[17] S. Chatterji. Mechanism of the $CaCl_2$ attack on portland cement concrete. *Cement and Concrete Research*, 8(4):461–467, 1978.

[18] K. Chenoweth, S. Cheung, A. C. T. van Duin, W. A. Goddard, and E. M. Kober. Simulations on the thermal decomposition of a poly(dimethylsiloxane) polymer using the reaxff reactive force field. *Journal of the American Chemical Society*, 127(19):7192–7202, 2005.

[19] S. Cheung, W. Deng, A. Duin, and W. Goddard. Reaxffmgh reactive force field for magnesium hydride systems. *J. Phys. Chem. A*, 109(5):851–859, 2005.

[20] T.-j. Chuang. *Nanomechanics of Materials and Structures.* 2006.

[21] D. A. Dikin, X. Chen, W. Ding, G. Wagner, and R. S. Ruoff. Resonance vibration of amorphous SiO_2 nanowires driven by mechanical or electrical field excitation. *Journal of Applied Physics*, 93(1):226–230, 2003.

[22] T. M. Dugdale, R. Dagastine, A. Chiovitti, and R. Wetherbee. Diatom adhesive mucilage contains distinct supramolecular assemblies of a single modular protein. *Biophys J*, 90(8):2987–93, 2006.

[23] A. Duin. Reaxff user manual. *http://www.wag.caltech.edu/home/duin/manual.html*, 2002.

[24] A. Duin, S. Dasgupta, F. Lorant, and W. Goddard. Reaxff: A reactive force field for hydrocarbons. *J. Phys. Chem. A.*, 105:9396, 2001.

[25] A. Duin, K. Nielson, W. Deng, J. Oxgaard, and W. Goddard. Application of reaxff reactive force fields to transition metal catalyzed nanotube formation. *Abstr. Papers Am. Chem. Soc.*, 227:U1031, 2004.

[26] A. Duin, A. Strachan, S. Stewman, Q. Zhang, X. Xu, and W. Goddard. Reaxffsio: Reactive force field for silicon and silicon oxide systems. *J. Phys. Chem. A.*, 107:3803–3811, 2003.

[27] G. E. Fantner, E. Oroudjev, G. Schitter, L. S. Golde, P. Thurner, M. M. Finch, P. Turner, T. Gutsmann, D. E. Morse, H. Hansma, and P. K. Hansma. Sacrificial bonds and hidden length: Unraveling molecular mesostructures in tough materials. *Biophysical Journal*, 90(4):1411–1418, 2006.

[28] W. Fenical. Plants: the potentials for extracting protein, medicines, and other useful chemicals: workshop proceedings. 1983.

[29] J. C. Fogarty, H. M. Aktulga, A. Y. Grama, A. C. T. van Duin, and S. A. Pandit. A reactive molecular dynamics simulation of the silica-water interface. *The Journal of Chemical Physics*, 132(17):174704, 2010.

[30] S. Fowler and N. Fisher. Viability of marine phytoplankton in zooplankton fecal pellets. *Deep Sea Res.*, 39(9):963–969, 1983.

[31] D. Fragoulis, M. G. Stamatakis, D. Papageorgiou, and E. Chaniotakis. The physical and mechanical properties of composite cements manufactured with calcareous and clayey greek diatomite mixtures. *Cement and Concrete Composites*, 27(2):205–209, Feb. 2005.

[32] A. Garcia and M. Buehler. Superductile, wavy silica nanostructures inspired by diatom algae. *in submission.*

[33] A. Garcia, D. Sen, and M. Buehler. Hierarchical silica nanostructures inspired by diatom algae yield superior deformability, toughness and strength. *under review*, review.

[34] A. P. Garcia and M. J. Buehler. Bioinspired nanoporous silicon provides great toughness at great deformability. *Computational Materials Science*, 48(2):303–309, 2010.

[35] I. C. Gebeshuber, J. H. Kindt, J. B. Thompson, Y. Del Amo, H. Stachelberger, M. Brzezinski, G. D. Stucky, D. E. Morse, and P. K. Hansma. Atomic force microscopy study of living diatoms in ambient conditions. *J. Microsc.-Oxf.*, 214:101–101, 2004.

[36] I. C. Gebeshuber, H. Stachelberger, and M. Drack. Diatom bionanotribology-biological surfaces in relative motion: Their design, friction, adhesion, lubrication and wear. *Journal of Nanoscience and Nanotechnology*, 5(1):79–87, 2005.

[37] A. Gilchrist and A. B. Gilchrist. *Life of William Blake, with selections from his poems and other writings.* Macmillan and co., 1880.

[38] C. Hamm and V. Smetacek. *Evolution of Primary Producers in the Sea.* Elsevier, Boston, 2007.

[39] C. E. Hamm, R. Merkel, O. Springer, P. Jurkojc, C. Maier, K. Prechtel, and V. Smetacek. Architecture and material properties of diatom shells provide effective mechanical protection. *Nature*, 421(6925):841–3, 2003.

[40] X. D. Han, K. Zheng, Y. F. Zhang, X. N. Zhang, Z. Zhang, and Z. L. Wang. Low-temperature in situ large-strain plasticity of silicon nanowires. *Adv. Mater.*, 19(16):2112, 2007.

[41] G. R. Hasle and E. E. Syvertsen. *Marine Diatoms.* Academic Press, San Diego, 1996.

[42] Hegel. *Lectures on the history of philosophy.* London: K. Paul, Trench, Trbner, & Co., 1892.

[43] M. Hildebrand. Diatoms, biomineralization processes, and genomics. *Chem Rev*, 108(11):4855–74, 2008.

[44] Y. H. Jing, Q. Y. Meng, and W. Zhao. Molecular dynamics simulations of the tensile and melting behaviours of silicon nanowires. *Physica E*, 41(4):685–689, 2009.

[45] W. L. Johnson. Bulk amorphous metal - an emerging engineering material. *JOM*, 54(3), 2002.

[46] O. Kayali, M. N. Haque, and B. Zhu. Some characteristics of high strength fiber reinforced lightweight aggregate concrete. *Cement and Concrete Composites*, 25(2):207–213, 2003.

[47] S. Keten, Z. Xu, B. Ihle, and M. J. Buehler. Nanoconfinement controls stiffness, strength and mechanical toughness of [beta]-sheet crystals in silk. *Nat Mater*, 9(4):359–367, 2010.

[48] D.-H. Kim, J.-H. Ahn, W. M. Choi, H.-S. Kim, T.-H. Kim, J. Song, Y. Y. Huang, Z. Liu, C. Lu, and J. A. Rogers. Stretchable and foldable silicon integrated circuits. *Science*, 320(5875):507–511, 2008.

[49] T. Y. Kim, S. S. Han, and H. M. Lee. Nanomechanical behavior of beta-sic nanowire in tension: Molecular dynamics simulations. *Mater. Trans.*, 45(5):1442–1449, 2004.

[50] H. Kimizuka, S. Ogata, and Y. Shibutani. Atomistic characterization of structural and elastic properties of auxetic crystalline SiO_2. *physica status solidi (b)*, 244(3):900–909, 2007.

[51] R. Z. Kramer, J. Bella, B. Brodsky, and H. M. Berman. The crystal and molecular structure of a collagen-like peptide with a biologically relevant sequence. *Journal of Molecular Biology*, 311(1):131–147, 2001.

[52] N. Kroger. Prescribing diatom morphology: toward genetic engineering of biological nanomaterials. *Curr Opin Chem Biol*, 11(6):662–9, 2007.

[53] N. Kroger and N. Poulsen. Diatoms-from cell wall biogenesis to nanotechnology. *Annu. Rev. Genet.*, 42:83–107, 2008.

[54] H. Liang, M. Upmanyu, and H. Huang. Size-dependent elasticity of nanowires: Nonlinear effects. *Physical Review B*, 71(24):241403, 2005.

[55] T. Limin and et al. Self-modulated taper drawing of silica nanowires. *Nanotechnology*, 16(9):1445, 2005.

[56] E. Litchman, C. A. Klausmeier, and K. Yoshiyama. Contrasting size evolution in marine and freshwater diatoms. *Proceedings of the National Academy of Sciences*, 106(8):2665–2670, 2009.

[57] W. Liu, K. Zhang, H. Xiao, L. Meng, J. Li, G. M. Stocks, and J. Zhong. Surface reconstruction and core distortion of silicon and germanium nanowires. *Nanotechnology*, 18(21):215703, 2007.

[58] D. Losic, J. G. Mitchell, and N. H. Voelcker. Diatomaceous lessons in nanotechnology and advanced materials. *Adv. Mater.*, 21:112, 2009.

[59] D. Losic, R. J. Pillar, T. Dilger, J. G. Mitchell, and N. H. Voelcker. Atomic force microscopy (afm) characterisation of the porous silica nanostructure of two centric diatoms. *J Porous Mater*, 14, 2007.

[60] D. Losic, K. Short, J. G. Mitchell, R. Lal, and N. H. Voelcker. Afm nanoindentations of diatom biosilica surfaces. *Langmuir*, 23(9):5014–21, 2007.

[61] J. P. Lucas, N. R. Moody, S. L. Robinson, J. Hanrock, and R. Q. Hwang. Determining fracture toughness of vitreous silica glass. *Scripta Metallurgica et Materialia*, 32(5):743–748, 1995.

[62] N. Lundholm, j. Moestrup, G. R. Hasle, and K. Hoef-Emden. A study of the pseudo-nitzschia pseudodelicatissima/cuspidata complex (bacillariophyceae): What is p. pseudodelicatissima? *Journal of Phycology*, 39(4):797–813, 2003.

[63] H. Mehrez and S. Ciraci. Yielding and fracture mechanisms of nanowires. *Phys. Rev. B*, 56(19):12632, Nov. 1997.

[64] F. Musso, M. Sodupe, M. Corno, and P. Ugliengo. H-bond features of fully hydroxylated surfaces of crystalline silica polymorphs: A periodic b3lyp study. *The Journal of Physical Chemistry C*, 113(41):17876–17884, 2009.

[65] A. Nakano, R. K. Kalia, K. ichi Nomura, A. Sharma, P. Vashishta, F. Shimojo, A. C. van Duin, W. A. Goddard, R. Biswas, and D. Srivastava. A divide-and-conquer/cellular-decomposition framework for million-to-billion atom simulations of chemical reactions. *Computational Materials Science*, 38(4):642–652, 2007.

[66] T. Namazu and Y. Isono. Quasi-static bending test of nano-scale SiO_2 wire at intermediate temperatures using afm-based technique. *Sensors and Actuators A: Physical*, 104(1):78–85, 2003.

[67] H. Ni, X. Li, and H. Gao. Elastic modulus of amorphous SiO_2 nanowires. *Applied Physics Letters*, 88(4):043108–3, 2006.

[68] K. Nielson, A. Duin, J. Oxgaard, W. Deng, and W. Goddard. Development of the reaxff reactive force field for describing transition metal catalyzed reactions with application to the initial stages of the catalytic formation of carbon nanotubes. *J. Phys. Chem. A.*, 109(3):493–499, 2005.

[69] H. S. Park. Quantifying the size-dependent effect of the residual surface stress on the resonant frequencies of silicon nanowires if finite deformation kinematics are considered. *Nanotechnology*, 20(11):115701, 2009.

[70] N. Poulsen and N. Kroger. Silica morphogenesis by alternative processing of silaffins in the diatom thalassiosira pseudonana. *J Biol Chem*, 279(41):42993–9, 2004.

[71] T. V. Ramachandra, D. M. Mahapatra, K. B, and R. Gordon. Milking diatoms for sustainable energy: Biochemical engineering versus gasoline-secreting diatom solar panels. *Industrial & Engineering Chemistry Research*, 48(19):8769–8788, 2009.

[72] A. Rappe and W. Goddard. Charge equilibration for molecular dynamics simulations. *J. Phys. Chem. A*, 95(8):3358–3363, 1991.

[73] J. A. Raven and A. M. Waite. The evolution of silicification in diatoms: inescapable sinking and sinking as escape? *Tansley review*, 162:45–61, 2003.

[74] D. Raymand, A. C. van Duin, M. Baudin, and K. Hermansson. A reactive force field (reaxff) for zinc oxide. *Surface Science*, 602(5):1020–1031, Mar. 2008.

[75] F. Round, R. M. Crawford, and D. G. Mann. *Diatoms: Biology and Morphology of the Genera.* Cambridge University Press, 1990.

[76] C. Rountree, S. Prades, D. Bonamy, E. Bouchaud, R. Kalia, and C. Guillot. A unified study of crack propagation in amorphous silica: Using experiments and simulations. *Journal of Alloys and Compounds*, 434-435:60–63, May 2007.

[77] H. C. Schroder, X. Wang, W. Tremel, H. Ushijima, and W. E. Muller. Biofabrication of biosilica-glass by living organisms. *Nat Prod Rep*, 25(3):455–74, 2008.

[78] D. Sen and M. J. Buehler. Chemical complexity in mechanical deformation of metals. *Int. J. Multiscale Comput. Eng.*, 5:181–202, 2007.

[79] E. Silva, J. Li, D. Liao, S. Subramanian, T. Zhu, and S. Yip. Atomic scale chemo-mechanics of silica: Nano-rod deformation and water reaction. *Journal of Computer-Aided Materials Design*, 13(1):135–159, 2006.

[80] E. Silva, L. Tong, S. Yip, and K. Van Vliet. Size effects on the stiffness of silica nanowires. *Small*, 2(2):239–243, 2006.

[81] B. L. Smith, T. E. Schaffer, M. Viani, J. B. Thompson, N. A. Frederick, J. Kindt, A. Belcher, G. D. Stucky, D. E. Morse, and P. K. Hansma. Molecular mechanistic origin of the toughness of natural adhesives, fibres and composites. *Nature*, 399(6738):761–763, 1999.

[82] B. Stewart and P. Tait. *The Unseen universe: or, Physical speculations on a future state.* Macmillan, 1875.

[83] A. Strachan, A. Duin, D. Chakraborty, S. Dasgupta, and W. Goddard. Shock waves in high-energy materials: The initial chemical events in nitramine rdx. *Phys. Rev. Lett.*, 91(9), 2003.

[84] M. Sumper. A phase separation model for the nanopatterning of diatom biosilica. *Science*, 295(5564):2430–2433, 2002.

[85] M. Sumper and E. Brunner. Learning from diatoms: Nature's tools for the production of nanostructured silica. *Adv. Funct. Mater*, 16:1726, 2006.

[86] M. Sumper and G. Lehmann. Silica pattern formation in diatoms: Species-specific polyamine biosynthesis. *ChemBioChem*, 7(9):1419–1427, 2006.

[87] G. Sutmann. John von neumann institute for computing. *Classical Molecular Dynamics*, 10:211–254, 2002.

[88] Z. L. Wang, R. P. Gao, P. Poncharal, W. A. de Heer, Z. R. Dai, and Z. W. Pan. Mechanical and electrostatic properties of carbon nanotubes and nanowires. *Materials Science and Engineering: C*, 16(3):3–10, 2001,.

[89] Wipeter. Circle of diatoms on a slide. *http://en.wikipedia.org/wiki/Diatom*, 2009.

[90] B. Wu, A. Heidelberg, J. J. Boland, J. E. Sader, Sun, and Li. Microstructure-hardened silver nanowires. *Nano Letters*, 6(3):468–472, 2006.

[91] C. Yi, D. Liu, and M. Yang. Building nanoscale architectures by directed synthesis and self-assembly. *Current Nanoscience*, 5:75–87, 2009.

[92] W. W. Zhang, Q. A. Huang, H. Yu, and L. B. Lu. Size-dependent Elasticity of Silicon Nanowires. In Wang, X, editor, *Micro and nano technology: 1st international conference of Chinese society of micro/nano technology (CSMNT)*, volume 60-61 of *Avanced Materials Research*, pages 315–319, Laublsrutistr 24, Ch-8717 Stafa-Zurich, Switzerland, 2009. Chinese Soc Micro Nano Technol; Tsinghua Univ; China Natl Acad Nanotechnol & Engn; State Key Lab Precis Measure Technol & Instruments; State Key Lab Tribol, Trans Tech Publications Ltd. 1st

International Conference of Chinese-Society-of-Micro-Nano-Technology, Beijing, Peoples R China, Nov 19-22, 2008.

[93] T. Zhu, J. Li, S. Yip, R. J. Bartlett, S. B. Trickey, and N. H. de Leeuw. Deformation and fracture of a SiO_2 nanorod. *Molecular Simulation*, 29(10):671 – 676, 2003.

[94] J. A. Zimmerman and et al. Calculation of stress in atomistic simulation. *Modelling and Simulation in Materials Science and Engineering*, 12(4):S319, 2004.